RESEARCH ARTICLE

Key Points:
- NEMOMED12 is able to reproduce a realistic deep water formation event in 2012–2013
- Ocean internal variability modulates half of the deep water formation area but it impacts marginally the integral deep water formation rate
- An ensemble simulation framework is necessary to evaluate accurately deep water formation in numerical ocean models

Supporting Information:
- Supporting Information S1
- Supporting Information S2
- Supporting Information S3
- Supporting Information S4

Correspondence to:
R. Waldman,
robin.waldman@meteo.fr

Modeling the intense 2012–2013 dense water formation event in the northwestern Mediterranean Sea: Evaluation with an ensemble simulation approach

Robin Waldman [1], Samuel Somot[1], Marine Herrmann[2], Anthony Bosse[3], Guy Caniaux [1], Claude Estournel [4], Loic Houpert [5], Louis Prieur[6], Florence Sevault[1], and Pierre Testor[3]

[1]Centre National de Recherches Meteorologiques (CNRM), Meteo-France-CNRS, UMR 3589, Toulouse, France, [2]Laboratoire d'Etudes Geophysiques et d'Oceanographie Spatiale (LEGOS), UMR5566, CNRS-Universite de Toulouse, Toulouse, France, [3]Laboratoire d'Oceanographie et de Climat-Experimentations et Approches Numeriques (LOCEAN), Centre National de Recherches Scientifiques (CNRS), Universite Pierre et Marie Curie (UPMC), Paris, France, [4]Laboratoire d'Aerologie (LA), CNRS-Universite de Toulouse, Toulouse, France, [5]The Scottish Association for Marine Science (SAMS), Oban, Scotland, UK, [6]Laboratoire d'Oceanographie de Villefranche-sur-Mer, Villefranche-sur-Mer, France

Abstract The northwestern Mediterranean Sea is a well-observed ocean deep convection site. Winter 2012–2013 was an intense and intensely documented dense water formation (DWF) event. We evaluate this DWF event in an ensemble configuration of the regional ocean model NEMOMED12. We then assess for the first time the impact of ocean intrinsic variability on DWF with a novel perturbed initial state ensemble method. Finally, we identify the main physical mechanisms driving water mass transformations. NEMOMED12 reproduces accurately the deep convection chronology between late January and March, its location off the Gulf of Lions although with a southward shift and its magnitude. It fails to reproduce the Western Mediterranean Deep Waters salinification and warming, consistently with too strong a surface heat loss. The Ocean Intrinsic Variability modulates half of the DWF area, especially in the open-sea where the bathymetry slope is low. It modulates marginally (3–5%) the integrated DWF rate, but its increase with time suggests its impact could be larger at interannual timescales. We conclude that ensemble frameworks are necessary to evaluate accurately numerical simulations of DWF. Each phase of DWF has distinct diapycnal and thermohaline regimes: during preconditioning, the Mediterranean thermohaline circulation is driven by exchanges with the Algerian basin. During the intense mixing phase, surface heat fluxes trigger deep convection and internal mixing largely determines the resulting deep water properties. During restratification, lateral exchanges and internal mixing are enhanced. Finally, isopycnal mixing was shown to play a large role in water mass transformations during the preconditioning and restratification phases.

1. Introduction

The Northwestern Mediterranean Sea (NWMed) is a key region of Dense Water Formation (DWF) in the World ocean [*Marshall and Schott*, 1999]. DWF and in particular the formation of Western Mediterranean Deep Water (WMDW), the main deep water mass in the Western Mediterranean Sea, constrains many biogeochemical and thermodynamical processes: nutrient renewal in upper layers and biological activity [*Tamburini et al.*, 2013; *Herrmann et al.*, 2014; *Auger et al.*, 2014], carbon and heat storage rate [*Santinelli et al.*, 2013; *Winton et al.*, 2013; *Rugenstein et al.*, 2013], and therefore climate.

DWF has long been observed in the NWMed Sea [*MEDOC-Group*, 1970; *Leaman and Schott*, 1991; *Schott et al.*, 1996; *Durrieu de Madron et al.*, 2013], mostly off the Gulf of Lions in an area centered on the "MEDOC" point (42°N,5°E). It is triggered in the winter by the cold and dry regional winds Mistral and Tramontane [*Leaman and Schott*, 1991; *Mertens and Schott*, 1998, *Somot et al.*, 2016]. It is typically described in three phases [*Marshall and Schott*, 1999]: the preconditioning phase, the intense mixing phase, and the restratification-spreading phase. During preconditioning, the DWF area shows an isopycnal dome and a cyclonic circulation that favors deep convection. During the intense mixing phase, the residual buoyancy of the whole water column is canceled by strong atmospheric fluxes and a deep convective mixed patch is formed. Finally, during the restratification-spreading phase, a mean overturning circulation is activated which exports newly-formed WMDW, imports lighter surrounding waters and increases the DWF area

buoyancy. This sequence is a conceptual view of the deep convection process and one should consider these three phases can overlap.

Several numerical case studies have been performed on observed DWF events, mostly the 1986–1987 [*Demirov and Pinardi*, 2007; *Herrmann et al.*, 2008; *Herrmann and Somot*, 2008], 2004–2005 [*Herrmann et al.*, 2010; *Beuvier et al.*, 2012], and 2012–2013 [*Estournel et al.*, 2016a; *Leger et al.*, 2016] events. They aimed at evaluating the deep convection simulated by numerical models and documenting the key processes that drive it. They have focused on the roles of atmospheric forcing [*Herrmann and Somot*, 2008; *Herrmann et al.*, 2010; *Estournel et al.*, 2016a], ocean preconditioning [*Herrmann et al.*, 2010; *Leger et al.*, 2016], model resolution [*Herrmann et al.*, 2008], and spreading [*Demirov and Pinardi*, 2007; *Beuvier et al.*, 2012] in those DWF events. In the period 2012–2013, an intense set of observations were carried out [*Estournel et al.*, 2016b] and results suggest that winter 2013 DWF event had an exceptional magnitude [*Waldman et al.*, 2016; *Houpert et al.*, 2016] (M. Herrmann et al., Long term interannual monitoring of open-ocean deep convection using altimetry and ocean color multi-sensors satellite data: Case study of the northwestern mediterranean sea, in revision). Therefore, in this study, we evaluate the representation of this DWF period in a regional ocean model.

Past numerical studies have focused mostly on the impact of atmospheric forcing and ocean preconditioning on the NWMed Sea DWF phenomenon. A large consensus emerges on the dominant role of atmospheric forcing in triggering DWF [*Demirov and Pinardi*, 2007; *Herrmann and Somot*, 2008; *Sannino et al.*, 2009; *Herrmann et al.*, 2010; *Béranger et al.*, 2010; *L'Hévéder et al.*, 2013; *Somot et al.*, 2016]. Several studies also point out the impact of ocean preconditioning before the convection event in modulating the DWF intensity [*Herrmann et al.*, 2010; *L'Hévéder et al.*, 2013; *Leger et al.*, 2016; *Somot et al.*, 2016]. For the 1986–1987 case study, *Herrmann et al.* [2010] find that preconditioning can modulate by a factor 2 the DWF rate, and *Leger et al.* [2016] find a factor 4.4 for the 2012–2013 case study, but in both cases the atmospheric forcing triggers the DWF event. At the interannual timescale, *L'Hévéder et al.* [2013] use a preconvection Index of Stratification (IS) as an interannual predictor of the DWF rate and *Somot et al.* [2016] also conclude on the dominant role of atmospheric forcing at those timescales.

Ocean preconditioning is likely to be impacted by the Ocean Intrinsic Variability (OIV), which none of the aforementioned study has quantified. The NWMed Sea is a strong eddying region [*Escudier et al.*, 2013] with instabilities of the Northern Current, the North Balearic Front [*Millot and Taupier-Letage*, 2005], and a large presence of mesoscale [*Gascard*, 1978] and submesoscale [*Testor and Gascard*, 2003] eddies. Those structures are a source of OIV [*Penduff et al.*, 2011] and can retroact on the basin-scale circulation through an inverse energy cascade [*Sérazin et al.*, 2015]. Recent numerical experiments have shown that this OIV contributes to 5–60% of the global thermohaline circulation variability [*Grégorio et al.*, 2015], being active from daily to multidecadal timescales [*Sérazin et al.*, 2015]. However, to our knowledge, the impact of OIV on DWF has not been assessed so far. Therefore, our study uses a regional ocean model to quantify the impact of OIV on DWF.

Finally, water mass transformation diagnostics have been largely used to relate water mass transformations to their thermohaline forcing [*Walin*, 1982]. This diagnostic was first performed as a function of S [*Walin*, 1977] and then of θ [*Walin*, 1982]. Since then, it has been a widely used diagnostic for both ocean observation and modeling. Its applications include transformations as a function of σ_0 [*Tziperman*, 1986; *Speer and Tziperman*, 1992; *Tziperman and Speer*, 1994; *Iudicone et al.*, 2008; *Badin et al.*, 2013], transformations in the nutrient concentration space [*Badin et al.*, 2010], transformations in the (θ,S) plane [*Speer*, 1993; *Groeskamp et al.*, 2014a; *Hieronymus et al.*, 2014], transformation maps showing areas of surface water mass formations [*Maze et al.*, 2009], conversion between wind-induced entrainment and water mass transformations [*Nilsson*, 1996], and DWF rate estimates in deep convection areas [*Myers and Donnelly*, 2008; *Waldman et al.*, 2016]. In the northwestern Mediterranean, *Tziperman and Speer* [1994] used this diagnostic to estimate the surface DWF rate and later *Herrmann et al.* [2008] identified the key role of lateral transports in the dense water export, light water import, and resulting overturning cell activated by deep convection. However, no clear role of internal mixing on water mass transformations has been established and the focus has been solely on diapycnal transformations whereas isoneutral surfaces are a preferred direction of mixing by basin-scale ocean turbulence [*Iselin*, 1939; *McDougall*, 1987; *McDougall et al.*, 2014]. We therefore aim in this study at identifying the main mechanisms of water mass transformations during DWF, with a special focus on internal and isopycnal transformations.

To summarize, this study evaluates NEMOMED12 regional ocean model's representation of the well-documented 2012–2013 DWF event, it quantifies the impact of OIV on DWF and it characterizes the water mass transformation processes at play. Section 2 describes the model, data, and methods used, section 3 presents the main results, section 4 discusses hypotheses, limitations, and perspectives, and section 5 summarizes the main conclusions.

2. Model, Data, and Methods

2.1. Model

We use the ocean general circulation model NEMO [*Madec*, 2008] in a regional configuration of the Mediterranean Sea called NEMOMED12 (Figure 1). See *Hamon et al.* [2016] for a similar configuration of this regional model. Its horizontal resolution is $\delta x = 6.1 - 7.1$ km in the NWMed Sea and it has 75 vertical levels of resolution between 1 m at the surface and 130 m at the bottom. In the NWMed Sea, the size of mesoscale eddies and meanders is typically between 30 and 80 km [*Crepon et al.*, 1982; *Millot*, 1991], but it is variable over time and space and the first baroclinic Rossby radius was estimated to be as low as 1.2 km in the DWF area during winter 2012–2013 (H. Giordani et al., A pv-approach for dense water formation along fronts: Application to the northwestern mediterranean, in revision). The model's far-dissipation range is $7\delta x = 42.5 - 50.0$ km [*Marchesiello et al.*, 2011], it is [*Marchesiello et al.*, 2011], it is therefore a mesoscale its bathymetry is extracted from MERCATOR-LEGOS version 10 $1/120°$ resolution database [*Beuvier et al.*, 2012].
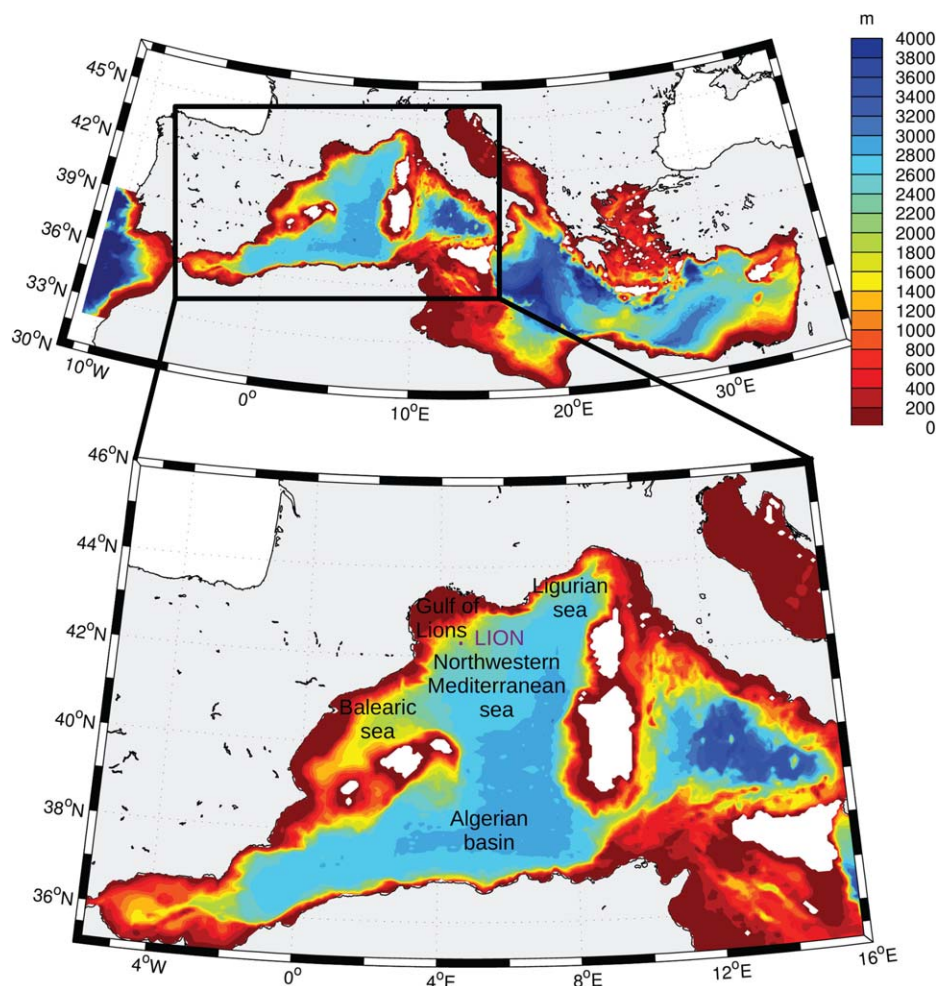

Figure 1. Domain and associated bathymetry for NEMOMED12 model. The (purple) locations of LION buoy and the (black) main basins are also displayed.

In terms of physics, we use in the horizontal a bilaplacian momentum diffusion operator ($-1.25{\times}10^{10}\,\text{m}^4/\text{s}$) to limit model diffusion at mesoscale. For tracers, we use a Laplacian isoneutral diffusivity operator ($60\,\text{m}^2/\text{s}$) to parametrize mixing by unresolved eddies but no eddy-induced velocity parametrization [*Gent and McWilliams*, 1990] is added to permit the explicit resolution of baroclinic eddies. At the lateral boundaries, we use a free slip condition. In the vertical, mixing is driven by the Turbulent Kinetic Energy scheme [*Gaspar et al.*, 1990], by the parametrizations of convection and bottom friction. For convection, we use the Enhanced Vertical Diffusion scheme which imposes a vertical mixing coefficient of $10\,\text{m}^2/\text{s}$ on tracers and momentum when static instabilities occur. At the bottom, a quadratic friction is applied is applied [*Beuvier et al.*, 2012] which depends on the bottom mean and on a tidal eddy kinetic energy climatology [*Lyard et al.*, 2006].

NEMOMED12 is forced at the surface by a dynamical downscaling of the ERA-Interim reanalysis by the 12 km resolution atmosphere-only regional climate model ALADIN-Climate version 5 [*Colin et al.*, 2010; *Herrmann et al.*, 2011]. This forcing called ALDERA [*Hamon et al.*, 2016] provides momentum, water, and heat fluxes every 3 h over the 2012–2013 period. The heat flux is applied with a Newtonian sea surface temperature (SST) restoration of $40\,\text{W}/\text{m}^2/\text{K}$ which parametrizes coupling at the first order [*Barnier et al.*, 1995, 2006]. Appendix A provides an evaluation of ALDERA forcing for the period 1 August 2012 to 30 June 2013 at LION buoy and over the NWMed Sea. ALDERA is shown to be realistic in terms of surface parameters and chronology, but it overestimates the net heat loss mostly due to a latent heat flux overestimation during intense wind events.

West of the Gibraltar strait, we apply a Newtonian temperature, salinity, and sea level restoration toward ORAS4 reanalysis [*Balmaseda et al.*, 2013]. Finally, the river runoff climatology is taken from *Ludwig et al.* [2009] for the main river mouths listed in RivDis [*Vörösmarty et al.*, 1996]. The inputs of the other rivers are gathered and imposed as a coastal runoff in each coastal grid point. The Black Sea runoff climatology is deduced from *Stanev and Peneva* [2001]. All restoration and runoff terms are monthly mean time series.

We develop in this study a novel perturbed initial state NEMOMED12 ensemble with a procedure described and evaluated below. NEMOMED12 runs for the period 2012–2013 until 30 June 2013 in order to diagnose all three phases of deep convection: preconditioning, intense mixing, and restratification.

2.2. Data

The realism of the numerical simulations is assessed using an extensive set of observations. This study takes advantage of the exceptional measurement year of 2012–2013 in the NWMed Sea during which intensive observations were carried out to study DWF and its effect on the vernal bloom intensity. Thanks to MERMeX (Marine Ecosystems Response in the Mediterranean Experiment), HyMeX (Hydrological Cycle of the Mediterranean Experiment), the ASICS-MED project, and the long-term observational program MOOSE (Mediterranean Ocean Observing System for the Environment, http://www.moose-network.fr) a number of cruises has been carried out at the basin scale, each summer and during 2012–2013 Winter-Spring period with the DEWEX field cruises [*Testor et al.*, 2012, 2013; *Testor*, 2013; *Conan*, 2013], collecting an important data set together with the use of autonomous platforms (gliders, profiling floats, moorings).

Observations include LION buoy (G. Caniaux et al., An inverse method to derive surface fluxes from the closure of oceanic heat and water budgets: Application for the northwestern Mediterranean, in revision) and deep mooring [*Testor et al.*, 2016] in the DWF area (42.102°N 4.703°E, see Figure 1) that we use to evaluate the air-Sea fluxes and to follow the chronology of deep convection both at the surface and the bottom of the water column. The LION buoy, anchored at 4.703°E 42.10°N (Figure 1), provides all the near surface meteorological observables since 2001 (except precipitation) to estimate turbulent fluxes. Since 2012, the dataset includes radiative fluxes (incoming and shortwave radiation). The data were checked following the procedure described by Caniaux et al. (in revision), and hourly turbulent fluxes (latent and sensible heat fluxes, and wind stress) were computed with the COARE3.0 flux algorithm [*Fairall et al.*, 2003] for the period 1 August 2012 to 30 June 2013. Due to missing sequences of values and rejected data, the record of fluxes is limited to only 1808 hourly fluxes (over 8760).

We also use extensively a series of four basin-scale CTD ship measurements in summer 2012, winter 2013, spring 2013, and summer 2013 including 68–82 CTD casts [*Testor et al.*, 2012; *Testor*, 2013; *Conan*, 2013; *Testor et al.*, 2013, see *Waldman et al.* [2016] for their location]. We use them to estimate basin-scale properties of the NWMed sea: thermohaline and density properties, integral buoyancy, and mixed patch area and volume. The mixed patch area and volume estimates from winter 2013 measurements are little sensitive to

sensor intercalibration, we therefore added ARGO measurements [*ARGO*, 2000] to compute them (three floats sampled the mixed patch).

Finally, we deduce a DWF area estimate from all glider measurements between January and March 2013 (up to six gliders at the same time, *Bosse et al.* [2016]). They only cover the depth 0–1000 m but they constitute by far the largest in situ observation source for this DWF event: assuming a vertical profile frequency of 1/h, six gliders perform in 14 h more CTD casts than any of the basin-scale CTD ship measurements.

Several area and volume estimates are integrated over space: the DWF areas, volumes, and the diapycnal and thermohaline volume transformations. In all cases but the glider-based estimates, we extrapolate observations over space using a kriging method validated by *Waldman et al.* [2016] for dense water volume estimates. This method uses no model guess to ensure the independence of results with numerical simulations, for model evaluation purposes. For the glider-based DWF area estimate, we use an objective analysis method validated by *Bosse et al.* [2015]. All integrated estimates are provided for the whole NWMed Sea, except the dense water volume estimate computed in the open-sea ($H > 2000$ m).

2.3. Creation and Validation of the Ensemble Initial State

In this study, we develop a novel perturbed initialized ensemble generation approach in order to address the impact of OIV on DWF in a realistic configuration. NEMOMED12 is initialized on 1 August 2012 based on an ocean objective analysis [*Estournel et al.*, 2016a]. The first guess of the initial state is given by the MERCATOR-Ocean operational analysis. To improve the realism of the model initial conditions over the region of interest, 3-D corrections were added using MOOSE-GE summer 2012 cruise [*Testor et al.*, 2012] and ARGO [*ARGO*, 2000] data. As described by *Estournel et al.* [2016a], these corrections are computed by interpolating the differences of temperature and salinity between observations and the first guess. An anisotropic interpolation method was preferred as *Estournel et al.* [2016a] show an improved error correction along isopycnals.

We consider that this objective analysis is only valid at the basin-scale. Indeed, most of the mesoscale and smaller-scale structures were not sampled by any observation. In addition, most of the OIV occurs at mesoscale [*Sérazin et al.*, 2015], which motivates to perturb the mesoscale field to quantify the role of OIV on DWF. As a consequence, we create 10 perturbed initial hydrologies by extracting the basin-scale potential temperature θ_{BS} and salinity S_{BS} from 1 August 2012 of *Estournel et al.* [2016a] objective analysis and the mesoscale θ_{MS} and S_{MS} from 1 August of years between 1980 and 1989 of a twin hindcast NEMOMED12 similar to the free run in *Hamon et al.* [2016]. For each model vertical level, θ_{BS} and S_{BS} are obtained by averaging each field over slipping windows of ±50 km in longitude and latitude, and θ_{MS} and S_{MS} are the residual: $\theta_{MS} = \theta - \theta_{BS}$ and $S_{MS} = S - S_{BS}$. The largest mesoscale structures reach 80–100 km in the NWMed Sea [*Millot*, 1991], we therefore ensure that the entire mesoscale signal is included in θ_{MS} and S_{MS}.

Figure 2 displays the initial Index of Stratification (IS) of the water column deduced from θ_{BS} and S_{BS} of *Estournel et al.* [2016a] objective analysis together with its measurement in observations (summer 2012 cruise, dots) and the example of IS mesoscale perturbation at the ocean bed from 1 August 1985 of the twin NEMOMED12 hindcast simulation. The sum of both terms is the initial IS of one of the ensemble members. The IS is defined following *Herrmann et al.* [2008] as:

$$IS(-H) = -\frac{g}{\rho_0} \int_{-H}^{0} z \frac{\partial \sigma_0}{\partial z} dz$$

with g the gravity acceleration, ρ_0 the reference density, $-H$ the depth of the ocean bed, and σ_0 the ocean potential density. The potential density is referenced at surface to correct from the effect of pressure on temperature and to ensure a comparison to surface buoyancy fluxes. The basin-scale IS deduced from *Estournel et al.* [2016a] is highly realistic when compared to observations (Figure 2a), with similar average values (mean bias of 0.08 m^2/s^2, root mean square error of 0.21 m^2/s^2) and space patterns (space correlation of 0.85). The low IS in the Gulf of Lions plateau is related to low bathymetry. A basin-scale North-South pattern appears with a relatively low stratification in the North of the basin ($\sim$1 m^2/s^2), where DWF occurs and high in the South ($\sim$2$-$3 m^2/s^2), with warmer and fresher surface Atlantic Waters (AW). In addition, a higher IS is observed along most coasts ($\sim$1.5 m^2/s^2) which corresponds to veins of stratified AW advected by the NWMed boundary currents. The mesoscale IS anomaly (Figure 2b) is null on average over the NWMed Sea and $\pm$0.15 m^2/s^2, which is up to $\sim$1/4 of the basin-scale stratification, as found in previous studies [*Bosse et al.*, 2015].
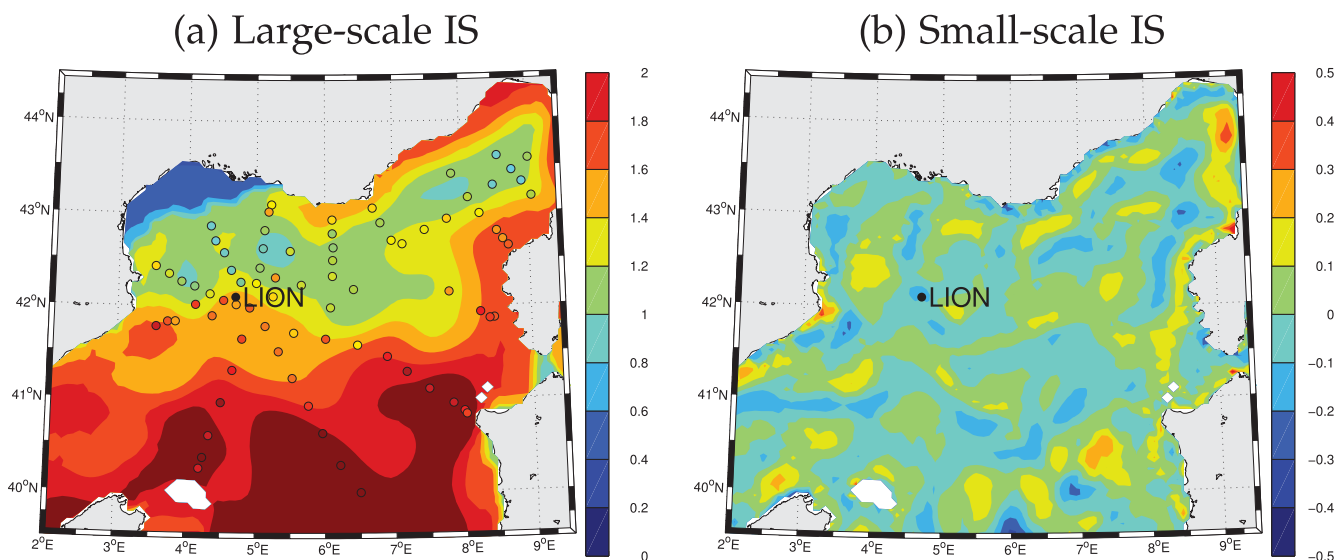
Figure 2. (a) Large-scale bottom stratification index ($IS(-H)$, m^2/s^2) common to all ensemble members, from *Estournel et al.* [2016] objective analysis; filled dots are observations from the summer 2012 cruise. (b) Mesoscale $IS(-H)$ anomaly used for one of the ensemble members, from 1 August 1985 of a NEMOMED12 hindcast simulation.

Figure 3 displays the average NWMed hydrological profiles on 1 August 2012 at observation locations (see the dots in Figure 2), in observations (black) and in the basin-scale initial state (blue), as well as its mean bias. The average observed hydrology allows to identify the three main water masses of the basin. At the surface, down to ~200 m depth is the AW, warm, and fresh. Its average salinity varies from 38.15 to 38.5 psu, with a minimum above 50 m depth, whereas its temperature varies highly from 13 to 23°C, with a seasonal thermocline of waters warmer than 15°C above 50m depth. The resultant potential density increases highly with depth between 26 and 29.02 kg/m^3. It implies that the IS increases sharply in the top 50 m that account for ~1/3 of the whole water column IS, and it reaches 1 m^2/s^2 at 200m depth, which accounts for most (70%) of the total IS. This means that the warm and fresh subsurface AW layer dominates the summer stratification in the NWMed Sea. Below, between ~200 and ~800 m depth are the LIW waters with a warm ($\theta > 13$°C) and salty ($S > 38.5$ psu) core, densities between 29.02 and 29.10 kg/m^3 and a low IS signature of 0.3 m^2/s^2 between the top and bottom of this layer. Finally, below ~800 m depth are the WMDW of almost constant temperature (12.9−13°C), salinity (38.47−38.50 psu), potential density (29.10−29.125 kg/m^3), and a low contribution to the integral stratification of 0.3 m^2/s^2, same as the LIW.

The basin-scale field has low biases with observations. The total and basin-scale initial states are very similar on average over the NWMed Sea (not shown), confirming that the mesoscale perturbations compensate over the domain. The spatial standard deviation (STD) of this mesoscale perturbation is 1.11°C and 0.08 psu for the AW, 0.03°C and 0.03 psu for the LIW, and 0.06°C and 0.01 psu for the WMDW (not shown). Temperature shows mostly a warm bias above 50 m depth, salinity shows a low fresh bias in the 30–100 m depth layer, which induces a light bias above 100 m depth and therefore a stratified bias down to 2000 m depth. However, this stratified bias represents 5−10% of the average stratification. In addition, the surface hydrology is extrapolated from 5 m depth to the surface in observations, which might cause part of this apparent bias. The ensemble average AW biases over the NWMed Sea reach +0.11°C, −0.01 psu, and −0.03 kg/m^3, LIW biases are +0.02°C, +0.01 psu, and −0.00 kg/m^3, and WMDW biases are all below 0.01°C, 0.01 psu, and 0.01 kg/m^3. For a comparison with other available products in the same period, the AW density bias is comparable in MEDRYS [*Hamon et al.*, 2016] and ASICS [*Leger et al.*, 2016] reanalyses, it is twice as high in MERCATOR (http://www.mercator-ocean.fr, *Leger et al.* [2016]) analysis and it is far higher (+0.2 kg/m^3) in the twin NEMOMED12 hindcast simulation (similar as *Hamon et al.* [2016] free run).

2.4. Methods
2.4.1. Deriving the Mixed Layer Depth From the IS
The IS allows to quantify the integral buoyancy of the water column, which resists to convection. It has the unit of a surface buoyancy flux, therefore it can be easily compared to atmospheric buoyancy fluxes. In this study, we use it for the first time to estimate the mixed layer depth (MLD). The MLD is determined as the depth where the IS reaches a threshold value of 0.01 m^2/s^2, which is of the order of the average daily

(a) Initial basin-scale hydrology

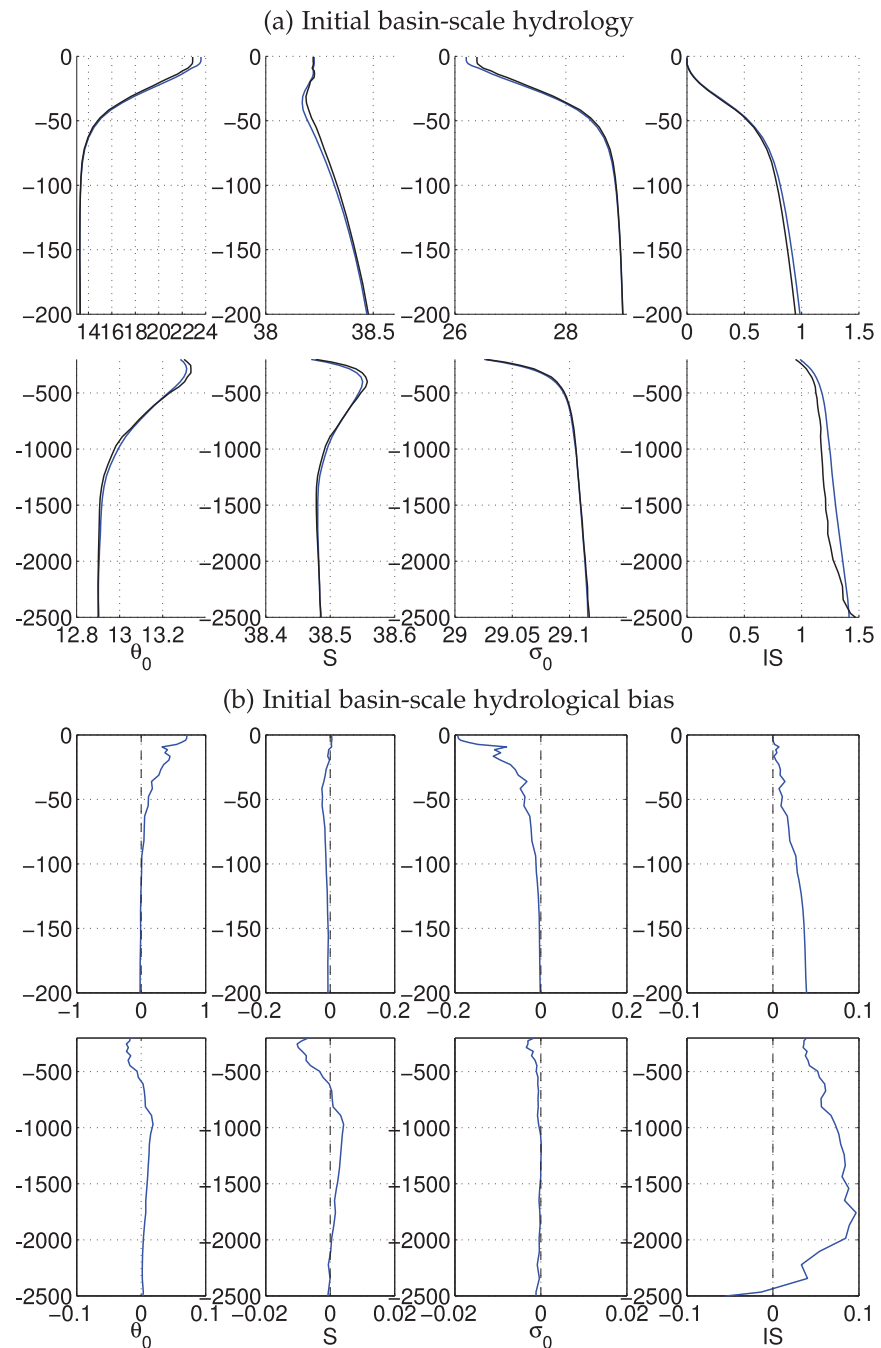(b) Initial basin-scale hydrological bias

Figure 3. (a: black) Average hydrological profiles from observations of the summer cruise 2012 and (blue) the model basin-scale initial state colocalized at observation locations. Salinity S (psu), temperature θ (°C), density σ_0 (kg/m^3), and the bottom index of stratification $(IS(-H))$ are displayed. (b) Same as Figure 3a for model biases.

surface buoyancy variation during winter [*Somot et al.* 2016; *Prieur et al.*, 2010]. Therefore, the mixed layer depth is physically determined as the surface layer whose stratification is canceled by a daily mean winter buoyancy loss. This allows to use a nonarbitrary physical criterion which is in relation with the surface forcing, contrary to density or temperature criteria.

2.4.2. Estimating the DWF Area and Rate

This study aims at quantifying the DWF rate in the NWMed basin-scale in NEMOMED12 and observations. For that we use three diagnostics: the convective mixed layer, the cold intermediate water area, and the dense water volume. We first estimate the mixed patch area and volume. The mixed patch is defined as the

area where $MLD > 1000$ m, which is the depth of the WMDW before the convective event (Figure 3). There-fore, when the mixed layer reaches this depth, its water has the properties of newly-formed WMDW. The area A_{MLD} in km^2 is integrated using the equation:

$$A_{MLD} = \iint_{MLD>1000} dxdy$$

This method has been largely used in previous studies [see *Waldman et al.*, 2016 for a review]. A convective volume V_{MLD} in m^3 can be deduced by multiplying A_{MLD} by the average MLD over the mixed patch:

$$V_{MLD} = \iint_{MLD>1000} MLD(x,y) dxdy$$

The second method estimates a convective area A_{cold} whose average θ between 400 and 600 m depth is $\theta_{400-600m} < 13°$C:

$$A_{cold} = \iint_{\theta_{400-600m}<13°C} dxdy$$

Indeed, once the warm intermediate water reaches the cold properties of the WMDW, it means that ocean convection has reached the isothermal depth of 1000 m (Figure 3). This indicator has already been used by *Somot et al.* [2016].

The last method quantifies the dense water volume and deduces a convective volume from its increase during deep convection. The dense water volume is defined as:

$$V_{29.11} = \iiint_{\sigma_0>29.11kg/m^3} dxdydz$$

Waldman et al. [2016] showed from observations that during the 2012–2013 DWF event, the DWF rate is maximal for $\sigma_0 = 29.11$ kg/m^3. This isopycnal thus quantifies the rate of renewal of dense waters for this year. Finally, a convective volume V_{dens} is deduced from the difference between the maximum $V_{29.11}$ during the intense mixing phase and its minimum during the preconditioning phase:

$$V_{dens} = max_{Int.Mix.}(V_{29.11}) - min_{Precond}(V_{29.11})$$

This method has been largely used in previous modeling studies [see *Waldman et al.* 2016 for a review]. Finally, V_{MLD} and V_{dens} can be converted into an equivalent annual volume flux F_{MLD} and F_{dens} in Sverdrup ($1Sv = 10^6$ m^3/s) by dividing the volume formed by the number of seconds in one year. F_{MLD} and F_{dens} are the equivalent deep water volume fluxes necessary to form the volumes, respectively, V_{MLD} and V_{dens} of deep water in one year, and they have been largely used to quantify DWF in the Mediterranean Sea [*Lascaratos*, 1993; *Castellari et al.*, 2000; *Somot et al.*, 2006; *Herrmann et al.*, 2008; *Beuvier et al.*, 2012]. We refer to them in the following as, respectively, the DWF rates and DWF volumes.

2.4.3. Water Mass Transformation Diagnostic

In this study, we assess water budgets as a function of θ, S, and σ_0. We first compute quantitative (θ,S) diagrams [*Montgomery*, 1958; *Worthington*, 1981] by displaying the NWMed basin water volume distribution, in % of the total volume, per (θ,S) bin.

In addition, we compute water mass transformation diagnostics as a function of θ [*Walin*, 1982], S [*Walin*, 1977], and σ_0 [*Tziperman and Speer*, 1994]. It is computed as a function of temperature and salinity for the first time in the Mediterranean Sea. The dense (respectively warm and salty) water volume as a function of σ_0 (respectively θ and S) is defined as:

$$V_{dens} = \iiint_{\sigma_0(x,y,z)>\sigma_0} dxdydz$$

The diapycnal (respectively diathermal and diahaline) transformation volume (DT, respectively TT and HT) between two dates d_1 and d_2 is:

$$DT = max_{\sigma_0}(|V_{dens}(d_2) - V_{dens}(d_1)|)$$

It quantifies the largest volume transformation in m^3 occurring in the σ_0 (respectively θ and S) dimension, which is particularly relevant during deep convection because it gives an estimate of the DWF magnitude [*Tziperman and Speer*, 1994; *Somot et al.*, 2006; *Herrmann et al.*, 2008].

We follow *Herrmann et al.* [2008] by decomposing the dense (respectively warm and salty) water volume tendency in the NWMed Sea (north of 40°N and west of 9°E) into four terms: a net volume variation V, a surface formation Su, a lateral transport T, and an interior mixing M, all in m^3 so that:

$$V = Su + T + M$$

Su quantifies the surface volume flux resulting from densification (respectively warming and saltening) by surface buoyancy (respectively heat and water) fluxes. T is computed from the lateral volume advection across the NWMed Sea boundaries: Spain – Menorca, Menorca – Sardinia, and Corsica - Ligurian coast. Finally, M is the residual from the formula $M = V - Su - T$. It includes all mixing processes occurring within the NWMed basin, both explicit and numerical.

3. Results

3.1. Chronology of the 2012–2013 Deep Convection Events

Figure 4 displays the evolution of atmospheric forcing ($|V|_{10m}$ and Q_{tot}), surface hydrology (SST, sea surface salinity SSS, and sea surface density $SS\rho$), and of the MLD at LION location in observations and in the NEM-OMED12 ensemble, between 1 December 2012 and 30 April 2013. The MLD is computed for model evaluation purposes with *Houpert et al.* [2016] method: a temperature threshold with respect to surface of 0.1°C down to 300 m depth, then of 0.01°C down to the bottom. The atmospheric forcing reveals strong winds on average ($|V|_{10m} \sim 10\,m/s$) and cooling at the surface over this period. A series of intense wind and cooling events related to the Mistral and Tramontane can be identified, with a wind exceeding 15 m/s and a surface cooling stronger than $-500\,W/m^2$ in early December, mid-January, throughout February and in mid-March, similar to modeling results from *Estournel et al.* [2016a]; and *Leger et al.* [2016]. Results from Annex 5 show that ALDERA represents well the chronology and geography of surface heat fluxes, but it overestimates strong coolings.
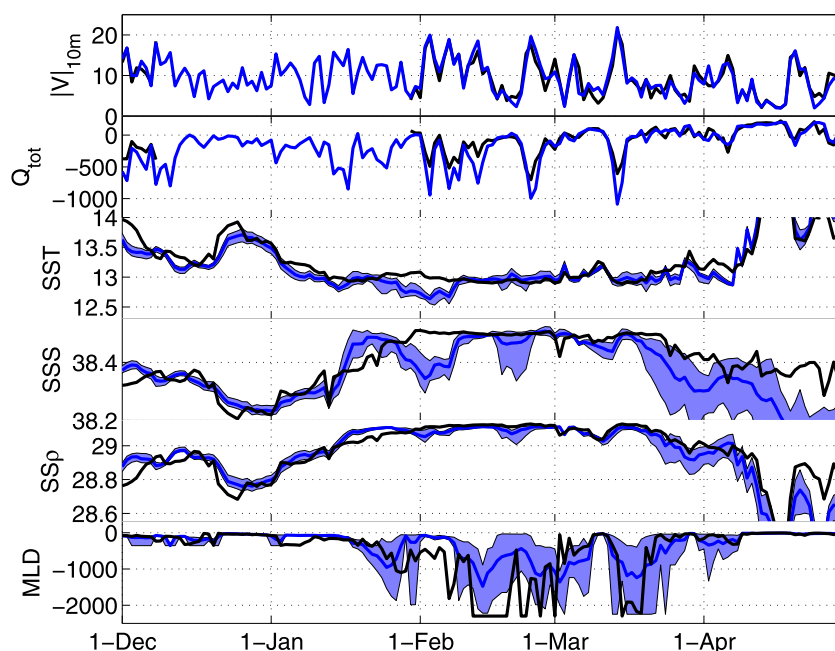

Figure 4. Daily time series of near-surface wind $|V|_{10m}$, net surface heat flux Q_{tot}, sea surface temperature (SST), salinity (SSS), and density ($SS\rho$) and of the mixed layer depth (MLD) at LION buoy between 1 December 2012 and 30 April 2013, (black) in observations when available and (blue) in NEMOMED12 ensemble. The bold lines represent the ensemble mean and the envelopes cover minimum and maximum values.

Those events are associated with a hydrological transition (Figure 4). The first step of convection between 23 December 2012 and 7 January 2013 is dominated by a cooling and a densification at the surface, with still low SSS and MLD: only the superficial AW are impacted by the air-sea interactions. In a second step, from 7 to 25 January, the SST stabilizes at ∼13°C whereas the SSS, $SS\rho$, and MLD increase to LIW values and depths of ∼38.5 psu, 29.10 kg/m³, and 300–800 m: convection starts to deepen to intermediate depth and the LIW layer is eroded. In a third step, occurring in the periods 26–28 January 2013, 6–28 February 2013, and 14–18 March 2013, the MLD increases to WMDW depth (>1000 m) and the surface hydrology stabilizes to the WMDW properties of ∼ 13.0°C, 38.48 psu, and 29.11 kg/m³.

This chronology is well-simulated on average by NEMOMED12, although the MLD is underestimated during the mid-February DWF event. Throughout the period, a high-frequency variability is visible in both observations and NEMOMED12, either inhibiting or enhancing deep convection, that can be related to the eddy advection from the meandering northern current located a few kilometers north [Crepon et al., 1982]. The eddy activity is confirmed by the large OIV. As a result NEMOMED12 biases are therefore largely insignificant, with the exception of the cold and fresh bias in early February. The MLD is the diagnostic that has the highest ensemble spread (between ∼200 and 2000 m), suggesting that DWF is a process that is particularly sensitive to OIV locally.

3.2. Estimating the Deep Convection Area

All basin-scale convection estimates are given in Table 1. Figure 5 displays A_{MLD} and A_{cold} surfaces in observations and in NEMOMED12 ensemble. Note that A_{MLD} estimate from observations integrates data from the winter 2013 cruise and ARGO profiles between 3 and 21 February 2013, whereas A_{cold} estimate is deduced from the January–March 2013 minimum $\theta_{400-600m}$ retrieved from glider profiles. Estimates in NEMOMED12 are computed at the same dates (blue) for evaluation purposes and as annual maxima (red) to assess the integrated modeled DWF area. First, A_{cold} and A_{MLD} surfaces are in agreement on a mixed patch location off the Gulf of Lions between $4-6°E$ and $41.2-42.8°N$, excluding slope areas. However, $A_{cold} > A_{MLD}$, which is consistent with the fact that A_{MLD} is only computed during the intense mixing phase, whereas A_{cold} is more integral in time. In addition, both diagnostics physically differ: A_{MLD} results solely from intense vertical mixing during the DWF events, whereas A_{cold} also results from the postconvection spreading of the convective intermediate waters. Figure 6 displays the daily series of A_{MLD} and A_{cold} in NEMOMED12 and the estimates from observations. In observations, $A_{MLD}=16,800$ km² and $A_{cold}=29,000$ km², confirming that $A_{cold} > A_{MLD}$.

The modeled DWF area at the observations dates (Figure 5, blue) covers the observed area but it extends further south to 41°N (A_{MLD}) and 40°N (A_{cold}) on average and marginally to the northeast. In addition, the northern extent of the DWF area is underestimated. The annual maximum DWF area in NEMOMED12 (red) is largely increased for A_{MLD}, especially to the south of the mixed patch and the Ligurian Sea, whereas A_{cold} is marginally increased. This confirms that in observations, A_{cold} estimate is more integrated in time than A_{MLD}. Now looking at the modeled A_{MLD} and A_{cold} time evolution, Figure 6 reveals a different behavior between both estimates. Whereas A_{MLD} is intermittent and decreases between the main intense mixing episodes, A_{cold} increases constantly throughout the intense mixing phase. A_{MLD} is derived from the MLD and gives an instantaneous estimate of convection which is maximal on 26 February 2013, whereas A_{cold} is integral in time and maximum on 20 March 2013. In NEMOMED12 ensemble, A_{MLD} and A_{cold} reach, respectively, $17,800 \pm 1,700$ and $45,000 \pm 1,700$ km² at the dates of observations. Therefore, NEMOMED12 simulates well A_{MLD}, however it overestimates A_{cold}.

We now look at the impact of OIV on DWF. We assess the ensemble dispersion by computing the mixed patch dispersive fraction (DF) which measures the fraction

Table 1. Large-Scale Estimates Related to the 2012–2013 Convective Event in Observations and NEMOMED12 Ensemble: Convection Area A_{MLD} and A_{cold} With Their Dispersive Fraction DF, Convection Volume V_{MLD} and $V_{29.11}$, Restratification Volume and The Diapycnal Transformation Volume (DT) for the Preconditioning (Before 5 January 2013), Intense Mixing (5 January 2013 to 24 March 2013), and Restratification (After 24 March 2013) Phases[a]

	Observations	NEMOMED12
A_{MLD} (km²)	16,800	$17,800 \pm 1,700$
A_{MLD} max (km²)	/	$28,000 \pm 900$
DF for A_{MLD} (%)	/	47
A_{cold} (km²)	29,000	$45,000 \pm 1,700$
DF for A_{cold} (%)	/	52
V_{MLD} (10¹³ m³)	2.4	3.4 ± 0.1
V_{MLD} max (10¹³ m³)	/	5.7 ± 0.2
V_{dens} (10¹³ m³)	4.5 ± 1.1	3.3 ± 0.2
V_{dens} max (10¹³ m³)	7.6 ± 1.6	5.4 ± 0.2
Restratification (10¹³ m³)	-2.6 ± 1.1	-1.4 ± 0.2
$DT_{precond}$ (10¹³ m³)	/	-2.4 ± 0.0
DT_{mix} (10¹³ m³)	/	5.8 ± 0.2
$DT_{restrat}$ (10¹³ m³)	/	-1.9 ± 0.2

[a]NEMOMED12 ensemble standard deviation is displayed when relevant.
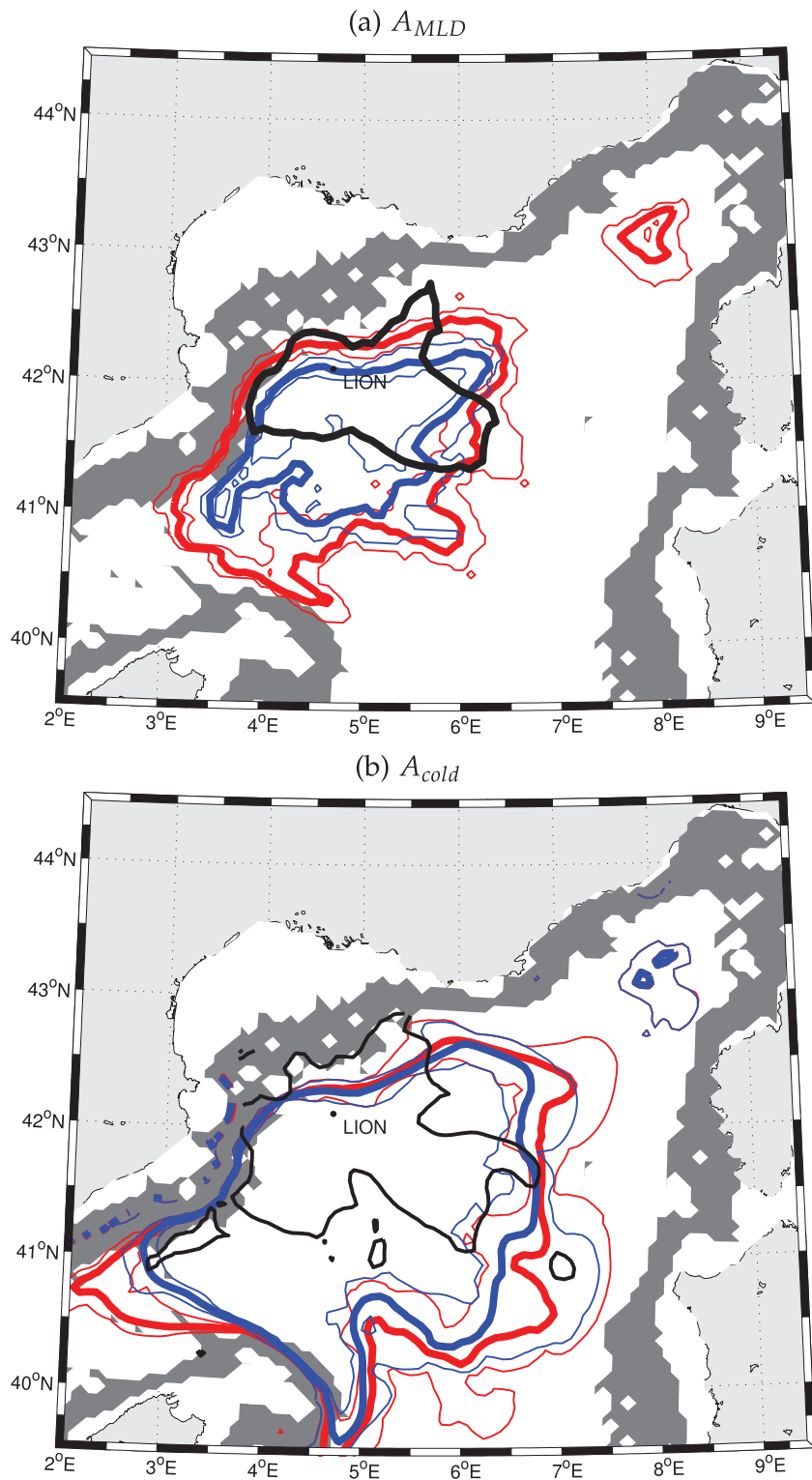
(a) A_{MLD}

(b) A_{cold}

Figure 5. (a: black) Convection area A_{MLD} in observations and (blue) NEMOMED12 ensemble at the dates of observations and (red) as an annual maximum. In NEMOMED12, (bold) the ensemble mean, (thin) minimum, and (thin) maximum areas are displayed (b) Convective area A_{cold}, with the same color code. Grey areas have a bathymetry slope higher than 2%.

between the dispersive mixed patch area (at least one member does not simulate DWF) and the total mixed patch area (at least one member simulates DWF): $DF = \frac{\max(A_{MLD}) - \min(A_{MLD})}{\max(A_{MLD})}$. Note that these surfaces are obtained from spatial composites of all members (Figure 5), so that: $\min(A_{MLD})$ is the area where all
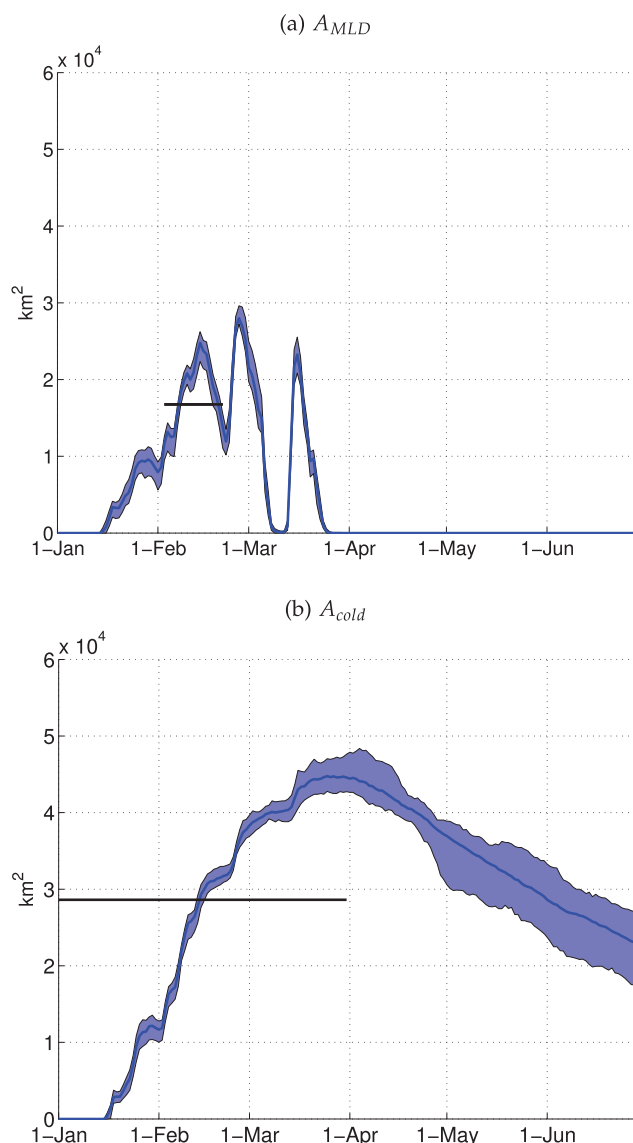
(a) A_{MLD}

(b) A_{cold}

Figure 6. (a: black) Convective area A_{MLD} as a function of time in observations and (blue) NEMOMED12 ensemble. The bold lines represent the ensemble mean and the envelopes cover minimum and maximum values. (b) Convective area A_{cold} as a function of time, with the same color code.

members simulate DWF, and max(A_{MLD}) is the area where at least one member simulates DWF. The DF reaches, respectively, 47 and 52% for A_{MLD} and A_{cold}. This means that over half of the total simulated mixed patch surface, at least two members disagree on the occurrence of deep convection. Therefore, about half of the DWF area is impacted by OIV. For both time maximum A_{MLD} and A_{cold} (Figure 6), the OIV is relatively low, with a STD below 5%. It means that the impact of OIV on DWF compensates over space on average. Such conclusions are in agreement with *Herrmann et al.* [2010] but in disagreement with *Leger et al.* [2016], however both studies perturb the basin-scale summer hydrology, which is expected to be mostly forced and less related to OIV [*Grégorio et al.*, 2015]. Finally, the OIV increases with time for A_{cold} and it is largest in spring: this suggests that it might play a larger role in DWF at interannual scales.

The 2% bathymetry slope (Figure 5) shows that areas least impacted by OIV are in the vicinity of the slope area. Indeed, the mixed patch northern extent is little impacted by OIV whereas its southern extent varies between 40.8 and 41.5°N among ensemble members and is therefore highly impacted by OIV. This suggests that the bathymetry slope inhibits the OIV. It is also visible in both mixed patch surface estimates from observations whose northern edges follow closely the 2% bathymetry slope contour. This result is consistent with results from ideali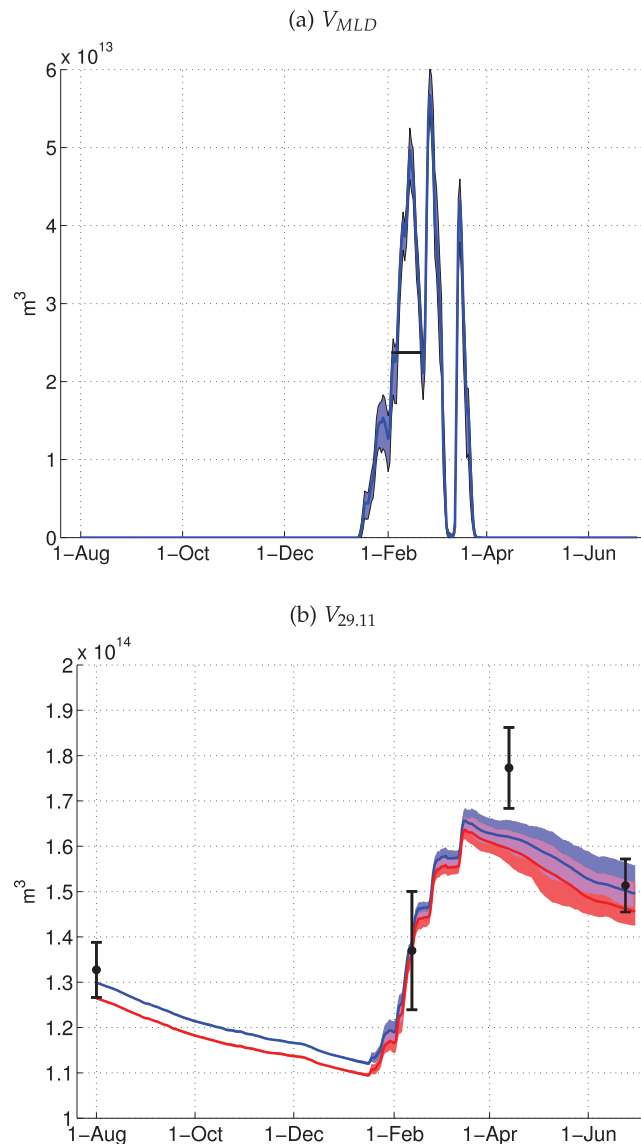zed simulations [*Spall*, 2004; *Pennel et al.*, 2012] which identify that the bathymetry slope inhibits boundary current instabilities and eddy fluxes between the shelf and the open-sea. *Spall* [2004] find using the linear quasi-geostrophic theory from *Blumsack and Gierasch* [1972] that cross-slope eddy fluxes are reduced by a factor 5 when the bathymetry slope is as large as the isopycnal slope, as compared to a flat bottom. Assuming that the OIV is related to eddy activity, consistently with results from *Penduff et al.* [2014], we conclude that the bathymetry slope inhibits the OIV of DWF in slope regions.

3.3. Estimating the DWF Volume and Rate

Figure 7 displays V_{MLD} and $V_{29.11}$ estimates in observations and their daily time series in NEMOMED12 in the NWMed Sea (blue) or in the open-sea ($H > 2000$ m, red). In observations, $V_{MLD} = 2.4 \times 10^{13}$ m^3, corresponding to an equivalent annual flux of $F_{MLD} = 0.75 Sv$. V_{dens} is deduced from the difference between $V_{29.11}$ in spring 2013 and $V_{29.11}$ in summer 2012 [see *Waldman et al.*, 2016 for more details] and it reaches the larger value of $V_{dens} = 4.5 \pm 1.1 \times 10^{13}$ m^3, corresponding to an annual flux of $F_{dens} = 1.4 \pm 0.3$ Sv. In addition, *Waldman*

(a) V_{MLD}

(b) $V_{29.11}$

Figure 7. (a: black) Convective volume V_{MLD} as a function of time in observations and (blue) NEMOMED12 ensemble. The bold lines represent the ensemble mean and the envelopes cover minimum and maximum values. (b) Dense water volume $V_{29.11}$ as a function of time, in the open-sea ($H > 2000$ m) for (black) observations and (red) NEMOMED12 and in the whole basin for (blue) NEMOMED12.

et al. [2016] suggested that the basin-integrated DWF volume could have reached $V_{dens} = 7.6 \pm 1.6 \times 10^{13}$ m³, corresponding to an equivalent annual flux of $F_{dens} = 2.3 \pm 0.5$ Sv. Similarly to A_{cold} and A_{MLD}, $V_{dens} > V_{MLD}$, which is consistent with the fact that V_{MLD} results from vertical mixing during deep convection, whereas $V_{29.11}$ also results from post-convection spreading. Such a discrepancy is also likely to be related to observation sampling issues.

NEMOMED12 ensemble shows convection volume evolutions similar to the convective area estimates: V_{MLD} is intermittent with a maximum on 26 February 2013 whereas $V_{29.11}$ increases throughout the intense mixing phase with a maximum on 17 March 2013. The ensemble $STD < 5\%$ for both estimates, confirming that the OIV impacts marginally the basin-scale DWF volume. Modeled V_{MLD} is overestimated by 46% in the observation period, but it shows a very large temporal variability which is likely to explain part of this bias. Its maximal value reaches an ensemble mean of $V_{MLD} = 5.7 \pm 0.2 \times 10^{13}$ m³ or $F_{MLD} = 1.8 \pm 0.1$ Sv on 26 February 2013. $V_{dens} = 5.4 \pm 0.2 \times 10^{13}$ m³ or $F_{dens} = 1.7 \pm 0.1$ Sv during the intense mixing phase (blue), however it is underestimated by 22%, reaching $V_{dens} = 3.6 \pm 0.2 \times 10^{13}$ m³ or $F_{dens} = 1.1 \pm 0.1$ Sv, at the dates of observations and in the open-sea ($H > 2000$ m, red). The modeled $V_{29.11}$ over the whole NWMed Sea (blue) is higher by 2.3% but it gives the same value for V_{dens}, confirming that in NEMOMED12, most of DWF occurs in the open-sea.

Now considering the upper estimate of $F_{dens} = 2.3 \pm 0.5$ Sv from *Waldman et al.* [2016], NEMOMED12 could underestimate the DWF rate by 29%. Finally the modeled $F_{dens} = 1.7 \pm 0.1$ Sv is very close to results from *Estournel et al.* [2016a] with a similar initial condition but different fluxes, and it is largely different from *Leger et al.* [2016] estimates which range from 0.59 to 2.59 Sv depending on the initialization of ocean summer preconditioning. Such differences are likely to be related to biases in the initial states used by *Leger et al.* [2016], as they use MERCATOR analysis which was shown to have biases twice as large as *Estournel et al.* [2016a] objective analysis on 1 August 2012.

Finally, the restratification volume is computed from the $V_{29.11}$ decrease between 13 April 2013 and 24 June 2013. In observations, it reaches $-2.6 \pm 1.1 \times 10^{13}$ m³, larger than NEMOMED12 (red) that reaches $-1.4 \pm 0.2 \times 10^{13}$ m³. Over the whole domain, NEMOMED12 restratification volume (blue) is even lower ($-1.2 \pm 0.2 \times 10^{13}$ m³), meaning that a fraction of the newly formed dense water volume is exported from

the open-sea to the slope and shelf area. The impact of OIV on restratification is larger in relative terms, reaching 14%. NEMOMED12 values are similar to those found by *Herrmann et al.* [2008] for the 1986–1987 case study at the eddy-permitting resolution.

3.4. Hydrological Signature of Convection
3.4.1. Quantitative Deep Water Transformations
Figure 8 displays the NWMed Sea quantitative (θ,S) diagram and the dense water volume V_{dens} on 1 August 2012, and their successive evolutions at the dates of the spring (13 April 2013) and summer (24 June 2013) cruises, in NEMOMED12 and observations. Note that for clarity purposes, only NEMOMED12 ensemble mean is displayed in Figures 8a–8c, an 8e. At the initial state (Figures 8a and 8b), deep water (θ,S) and σ_0 properties are similar in NEMOMED12 and observations (see Figure 3), therefore only NEMOMED12 ensemble mean is displayed. Most of the NWMed basin volume water hydrology is (12.88−12.92°C, 38.47−38.49 psu) and 29.105−29.12 kg/m^3, which corresponds to the WMDW properties preceeding the 2012–2013 convective event [*Durrieu de Madron et al.*, 2013]. Waters denser than 29.10 kg/m^3 account for 69% of the NWMed Sea volume, and those denser than 29.05 kg/m^3 account for 88% of it. Therefore, most of the NWMed Sea volume is displayed in Figures 8a and 8b. The observed dense water volume does not vary significantly between summer 2012 and winter 2013 cruises (Figure 7b), which is thus not displayed.

On 13 April 2013, after preconditioning, intense mixing and ∼3 weeks of restratification have occurred, the dense waters show an increasing density trend in both NEMOMED12 and observations (Figures 8c and 8d). Most of the volume increases occur between 29.11−29.125 kg/m^3. The observed DT (Figure 8d) reaches 4.5×10^{13} m^3, close to the NEMOMED12 value of 4.9±0.2×10^{13} m^3. The maximum diapycnal transformation is reached at 29.11 kg/m^3 in observations, whereas in NEMOMED12 ensemble it is reached at higher densities (29.116 kg/m^3). The impact of OIV on modeled DT is low (*STD*=8%). This confirms that OIV does not impact largely the basin-scale DWF in terms of hydrological transformation on an annual basis.

Quantitative (θ,S) transformations (Figure 8c) show a large difference between observations of a warming and saltening trend (∼+0.02°C, ∼ +0.01 psu), consistent with recent trends [*Schröder et al.*, 2006; *Durrieu de Madron et al.*, 2013] and a modeled cooling and saltening trend of (∼−0.02°C, ∼ +0.005 psu). The lack of warming signal in NEMOMED12 explains its bias in the newly formed WMDW density (Figure 8d.). It is consistent with the overestimation of surface cooling by ALDERA atmospheric forcing (see Appendix A). Also, the saltening trend is stronger in observations than NEMOMED12 despite a low initial salinity bias (Figure 3b) and a positive evaporation bias related to ALDERA forcing. Therefore, this fresh model bias does not result from local forcing. We found (not shown) that this fresh bias develops throughout the simulation as a signature of too fresh AW advected to the NWMed Sea. The cause for this bias is left for further studies. In NEMOMED12, a distinct volume of hydrology (12.9°C, 38.48 psu) in formed, of similar density as the preexisting WMDW (Figure 8c). Finally, in observations, waters lighter than 29.05 kg/m^3 also contribute to DWF whereas in NEMOMED12, the new WMDW results mostly from the densification of old WMDW of density $29.1 < \sigma_0 < 29.116$ (Figure 8d).

On 24 June 2013, after ∼10 more weeks of restratification, a fraction of the newly formed dense water has disappeared, mostly replaced by lighter WMDW and LIW (Figures 8e and 8f). In observations, half of the newly formed dense water has disappeared, representing a DT of 2.6×10^{13} m^3, replaced at ∼70% by lighter WMDW and at ∼25% by LIW. In NEMOMED12, the LIW lighter than 29.10 kg/m^3 contributes to most of the dense water replacement (Figure 8f.) and the DT is 54% lower (1.2×10^{13} m^3). Previous results [*Herrmann et al.*, 2008] have shown that eddy-permitting numerical models underestimate the destruction of new WMDW by export and mixing, which is likely to cause this bias. Finally, the OIV impact on the DT is of 14%, confirming its increase with time.

3.4.2. Deep Water Evolution at LION
Figure 9 displays the daily variation of S, θ, and σ_0 at the bottom of LION mooring (2300 m depth) in observations and NEMOMED12. We observe a saltening trend of ∼0.004 psu consistent with quantitative (θ,S) transformations (Figure 8c) mostly between early February and early March. Some high-frequency variability is visible during the intense mixing phase, possibly linked to eddy activity and/or internal waves [*Bosse et al.* 2016], but they are lower in amplitude than the saltening trend. The observed θ shows a long-term warming trend of ∼0.015°C throughout the period, also consistent with Figure 8c. However, the intense mixing

(a) 1-Aug-2012 (θ,S)
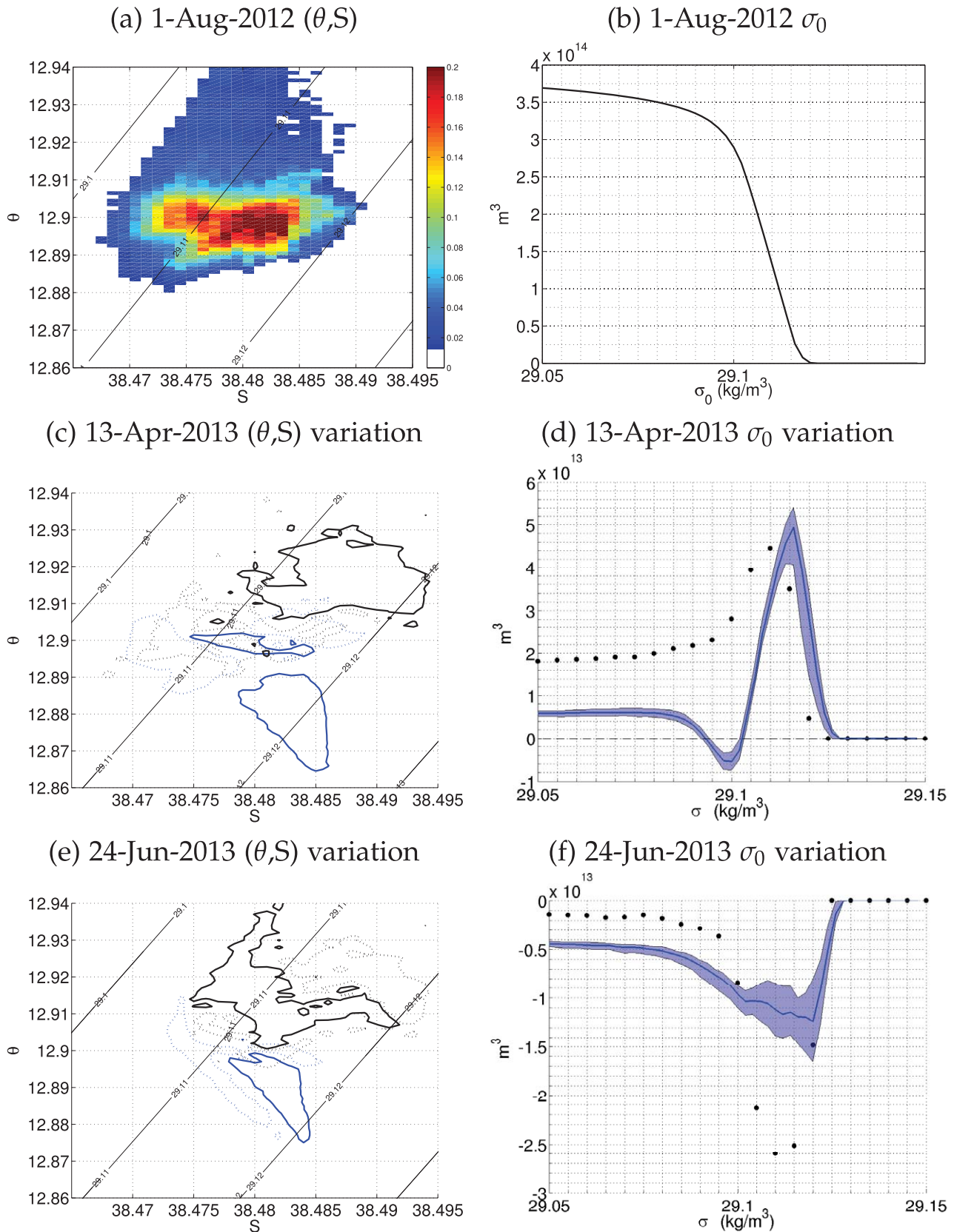
(b) 1-Aug-2012 σ_0

(c) 13-Apr-2013 (θ,S) variation

(d) 13-Apr-2013 σ_0 variation

(e) 24-Jun-2013 (θ,S) variation

(f) 24-Jun-2013 σ_0 variation
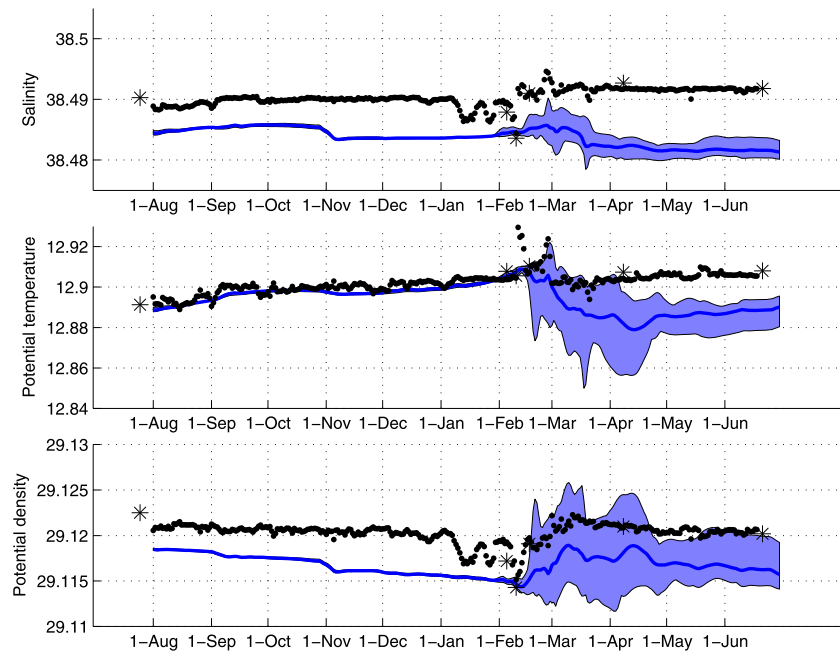
Figure 8.

Figure 9. Daily time series of sea bottom (2300 m depth) θ, S, and σ_0 at LION mooring in 2012–2013, in (black) observations and in (blue) NEMOMED12 ensemble. The bold lines represent the ensemble mean and the envelopes cover minimum and maximum values. Independent observations are displayed in dots (LION mooring) and stars (cruise measurements); an offset of -0.0052 psu has been applied to LION mooring data using intercalibrated cruise measurements.

phase is dominated by high-frequency variability and no clear temperature trend is visible in this period. Therefore, LION mooring suggests that the warming and saltening trend in Figure 8c. result from different mechanisms: a warming related the 2012 DWF event and a saltening during the 2013 DWF event. As a resultant, σ_0 slowly decreases before and after the intense mixing phase due to warming, whereas it increases rapidly ($\sim+0.003$ kg/m^3) in February due to saltening.

In NEMOMED12, a fresh (~-0.004 psu) and light (~-0.002 kg/m^3) bias is present before the intense mixing phase, but the temperature and its warming trend are remarkably well reproduced. A densification trend appears from 10 February 2013, in agreement with observations. It is mostly related to a cooling of $-0.02°$C, in agreement with Figure 8c. The corresponding densification is accurately simulated, in agreement with Figure 8d. We also note a freshening trend of -0.002 psu in NEMOMED12 during the intense mixing phase, related as argued before to the downward propagation during DWF of a fresh AW bias that develops throughout the simulation. The lack of a saltening signal at LION may be due to the weakness of this saltening and its space variability (Figure 8c). Finally, during the restratification phase, the long-term warming trend is again well reproduced by NEMOMED12.

The OIV is almost null until the DWF event starts, when it reaches values comparable to the ensemble mean signal in terms of θ and σ_0 ($STD=0.013°$C and 0.003 kg/m^3 on 28 February 2013). This means that OIV can largely impact the chronology and properties of DWF locally. This behavior was already visible at the surface of LION buoy (Figure 4) and in terms of the convective surface (Figure 5).

As a conclusion, the model evaluation confirms that NEMOMED12 reproduces realistically the well-documented and intense 2012–2013 DWF event. The chronology of the event is well-reproduced due to an accurate surface forcing chronology and summer ocean preconditioning. NEMOMED12 simulates a DWF mostly off the Gulf of Lions, in agreement with observations, but too much to the south. In terms of

Figure 8. (a) Quantitative (θ,S) diagram and (b) dense water volume from *Estournel et al.* [2016] basin-scale objective analysis on 1 August 2012. For the (θ,S) diagram, the volume fraction of the total NWMed ocean volume, in %, is displayed per (θ,S) class bin of resolution 10^{-3}psu and $10^{-3}°$C. (c,e) variations of the (θ,S) and (d,f) dense water volumes, respectively, between 1 August 2012 and 13 April 2013 and between 13 April 2013 and 24 June 2013. Observations are displayed in black, NEMOMED12 ensemble mean in blue, and the min-max envelope in light blue. For (c,e), only the $-0.05\%/0.001$ psu/0.001$°$ C (dotted) and $+0.05\%/0.001$ psu/0.001$°$ C (solid) contours are displayed.

intensity, despite divergent estimates from observations, NEMOMED12 shows the right order of DWF magnitude. In terms of hydrology, the WMDW densification is accurately reproduced and driven by a cooling in NEMOMED12 rather than a saltening in observations, which is consistent with too strong a latent heat loss induced by ALDERA. Finally, the OIV was shown to largely impact the geography of DWF and its hydrology locally, mostly in the open-sea, but it modulates marginally the integrated DWF rate. Several diagnostics also show an increase of OIV through time, especially during the intense mixing phase, suggesting its impact could be larger at interannual timescales.

3.5. Identification of Processes Driving Water Mass Transformations

Despite some biases, NEMOMED12 represents realistically the 2012–2013 DWF event. We now use it to identify the processes driving water mass transformations during deep convection by computing a water mass transformation diagnostic in σ_0, θ, and S dimensions. We decompose the 2012–2013 period into three DWF phases: preconditioning, intense mixing, and restratification. Intense mixing starts on 5 January 2013 when surface DWF (*Su*) at $\sigma_0 = 29.11\,\mathrm{kg/m^3}$ becomes nonnegligible in NEMOMED12, and it ends on 24 March 2013 when *Su* becomes negligible at this class. As a consequence, we define preconditioning between 1 August 2012 and 4 January 2013 and restratification between 25 March 2013 and 30 June 2013.

3.5.1. Preconditionning

Figure 10 displays NEMOMED12 ensemble mean hydrographic section with a schematic diagram of dominant water mass transformation processes for all phases of the deep convection phenomenon. Figure 11 displays water mass transformations in NEMOMED12, for the three phases of convection and as a function of σ_0, θ, and S. In terms of density, the preconditioning phase (Figure 11a) is dominated by the replacement of WMDW denser than $29.102\,\mathrm{kg/m^3}$ by lighter water, mostly (80–90%) LIW of density $29.08-29.10\,\mathrm{kg/m^3}$ ($DT = -2.4 \pm 0.0 \times 10^{13}\,\mathrm{m^3}$). The lateral transport T largely dominates the dense water budget through meridional exchanges with the Algerian basin between Menorca and Sardinia islands (not shown).

Transformations in the temperature and salinity dimensions (Figures 11d and 11g) also reveal the destruction of cold ($12.88-12.90°C$) and fresh ($38.46-38.48$psu) waters replaced by warmer ($12.90-13.7°C$) and saltier ($38.48-38.60$psu) waters, at a rate of $TT = 2.9 \pm 0.1 \times 10^{13}\,\mathrm{m^3}$ and $HT = 2.3 \pm 0.1 \times 10^{13}\,\mathrm{m^3}$. OIV is very low in all cases, suggesting that at that stage, it impacts marginally water mass transformations. However, those transformations are only dominated by transport in the range $12.92-13.70°C$ and $38.49-38.58$psu. Indeed, an intense internal mixing occurs at the hydrology of WMDW ($12.88-12.92°C$ and $38.46-38.49$psu) and for the saltiest LIW ($38.58-38.70$psu) which is responsible for the warming and saltening of WMDW. The maximum volume transformations induced by *Su* and *M* are similar, meaning that both processes drive the preconditioning phase. In addition, *M* has no density signature, it therefore corresponds to isopycnal mixing. The latter result is consistent with the domination of isopycnal mixing over diapycnal mixing in the world ocean [*Iselin*, 1939; *McDougall*, 1987; *McDougall et al.*, 2014]. In NEMOMED12, diapycnal mixing is parametrized through vertical turbulence and it can reach in the interior ocean its background value of $Kz_b = 10^{-5}\,\mathrm{m^2/s}$, whereas isopycnal mixing is resolved by mesoscale eddies and parametrized by a tracer diffusion coefficient of $Kh = 60\,\mathrm{m^2/s}$. The ratio between both diffusivity coefficients can therefore reach $Kh/Kz_b = 6 \times 10^6$ in the interior ocean. Such an isopycnal mixing between different WMDW might be the signature of the 2012 DWF event [*Durrieu de Madron et al.*, 2013] spreading phase that mixes new and old WMDW.

3.5.2. Intense Mixing

During the intense mixing phase, Figure 11b. shows a large DT of $5.8 \pm 0.2 \times 10^{13}\,\mathrm{m^3}$. The dense waters formed have densities between $29.114-29.128\,\mathrm{kg/m^3}$, confirming that the large densification signal visible for NEMOMED12 in Figure 8d occurs during the intense mixing phase. Most of the DWF is associated with the destruction of lighter WMDW, as ~65% of the water destroyed has $29.10 < \sigma_0 < 29.114\,\mathrm{kg/m^3}$. Now looking at the contributions to this intense mixing phase, the dominant term is the surface forcing *Su*, which confirms that ocean convection is triggered by surface fluxes. The surface term resembles the total volume variation, however its amplitude is higher, reaching $6.4 \times 10^{13}\,\mathrm{m^3}$, and it acts at higher densities. The interior mixing term is also large during this phase, although lower by a factor ~2 than surface forcing. It acts at denser levels than the surface term: it destroys totally the densest waters ($\sigma_0 > 29.118\,\mathrm{kg/m^3}$) formed at the surface and replaces them with slightly lighter WMDWs ($29.108 < \sigma_0 < 29.118\,\mathrm{kg/m^3}$). This implies that the new WMDW ultimately result from internal mixing. It might be related either to the vertical mixing during the mixed layer deepening, or to horizontal mixing at the mixed patch boundaries. Finally, lateral
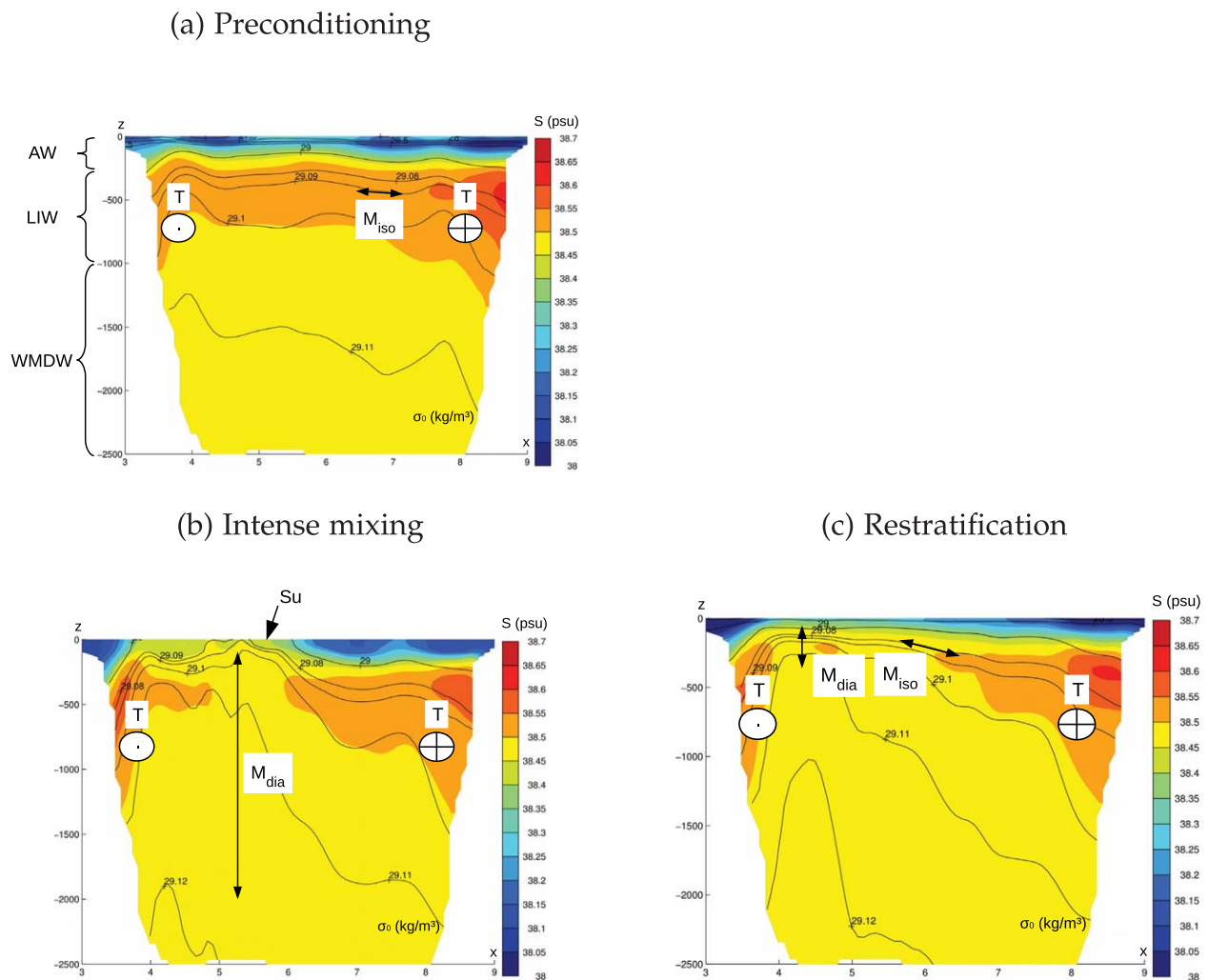
(a) Preconditioning

(b) Intense mixing

(c) Restratification

Figure 10. (a) Schematic diagram of the dominant water mass transformation processes during the preconditioning phase (1 August 2012 to 4 January 2013): transport T, internal mixing M, and surface fluxes Su. NEMOMED12 ensemble mean average hydrographic section at 41.5° N is displayed. The directions of transport (either incoming or outcoming) and mixing (either isopycnal or diapycnal) are displayed. The average vertical location of Atlantic Waters (AW), Levantine Intermediate Waters (LIW), and Western Mediterranean Deep Waters (WMDW) is also displayed. (b-c): same as Figure 10a for the intense mixing phase (5 January 2013 to 24 March 2013) and the restratification phase (25 March 2013 to 30 June 2013).

transport resembles highly its structure during preconditioning but it only contributes to a small fraction of dense water transformations during this phase.

The WMDW formation rate reaches similar values in temperature and salinity dimensions, with the formation of new WMDW at properties of $12.84-12.90°C$ and 38.48-38.51 psu. However, whereas Su plays a marginal role in diahaline transformations, it triggers large diathermal transformations: this illustrates that the DWF event is forced at the surface by thermal buoyancy fluxes. In addition, in both cases, internal mixing plays a central role in determining the resulting WMDW properties: it dominates all diahaline transformations and it counteracts surface diathermal fluxes to form waters between $12.84-13.16°C$ and destroy a large volume of LIW. T also has a similar structure to the preconditioning phase and plays a minor role. Finally, the ensemble dispersion is again low, although higher ($STD=0.2\times10^{13}$ m^3 for the DT, TT, and HT) than in the previous phase.

3.5.3. Restratification

Finally, during the restratification phase, Figure 11c shows the new WMDW destruction at $\sigma_0 > 29.12$ kg/m^3 and $DT=-1.9\pm0.2\times10^{13}$ m^3. They are replaced by all three main water masses of the basin: AW lighter than 29.05 kg/m^3 account for 35% of the replacement, LIW of $29.05 < \sigma_0 < 29.10$ kg/m^3 account for 40%, and finally lighter WMDW account for the remaining 25%. The surface term is negligeable by

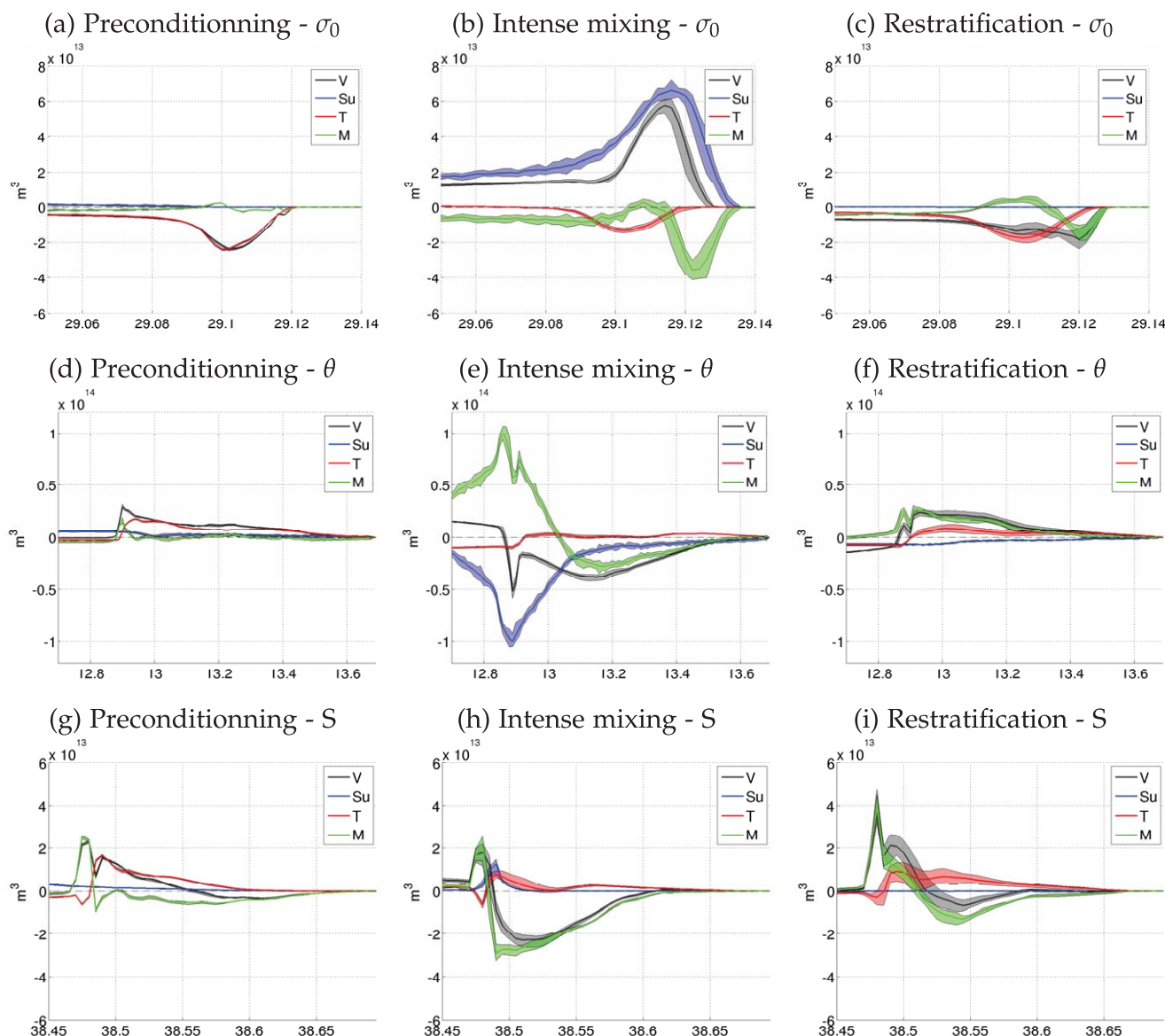**Figure 11.** (a–c) Evolution of the NWMed Sea dense water volume (V in m³) in NEMOMED12 as a function of σ_0 and contributions of surface fluxes (Su), lateral transport (T) and internal mixing (M) during (a) preconditioning (1 August 2012 to 4 January 2013), (b) intense mixing (5 January 2013 to 24 March 2013) and (c) restratification (25 March 2013 to 30 June 2013). The bold lines display the ensemble mean and the envelopes cover minimum and maximum values. (d–f) and (g–i): same as Figures 11a–11c for diathermal and diahaline transformations.

construction. Lateral transport is dominated by the meridional exchanges with the Algerian basin (not shown), it exports both old ($29.105-29.114\,\mathrm{kg/m^3}$) and new ($29.114-29.128\,\mathrm{kg/m^3}$) WMDW and it imports mostly LIW ($29.08-29.10\,\mathrm{kg/m^3}$). It is enhanced with respect to the preconditioning phase, being twice as large per day. Mixing destroys the densest WMDW and LIW waters to form lighter WMDW. As a resultant, most of the lighter WMDW of $29.105 < \sigma_0 < 29.120\,\mathrm{kg/m^3}$ exported to the Algerian basin are replaced in the NWMed by the internal mixing processes, and their volume remains almost constant during the restratification phase.

Transformations in the temperature and salinity dimensions (Figures 11f and 11i) are larger than diapycnal transformations, with $TT=2.4\pm0.2\times10^{13}\,\mathrm{m^3}$ and $HT=3.7\pm0.4\times10^{13}\,\mathrm{m^3}$. We also note the destruction of mostly WMDW with a cold ($12.84-12.86\,^\circ\mathrm{C}$) and fresh ($38.47-38.48\,\mathrm{psu}$) signature. It is replaced by two distinct water masses: warmer and saltier WMDW, and LIW. Thermohaline transformations reveal that internal mixing plays a large role in setting intermediate and deep water characteristics. Indeed, internal mixing

contributes to the formation of warmer ($12.88-12.90°$C) and saltier ($38.48-38.49$psu) WMDW and of colder ($13.16-13.40°$C) and fresher ($38.50-38.54$psu) LIW typical of the NWMed basin. Both internal mixing processes have a strong isopycnal component because they have little or no density signature. In addition, the volumes involved in diathermohaline mixing, and particularly diahaline mixing, are larger than diapycnal mixing. It means that during restratification, isopycnal internal mixing contributes to the dominant water mass transformations: the formation of WMDW and LIW waters resulting from the mixing of pre-existing waters. Finally, the ensemble dispersion is higher than in the two previous phases, showing that through time, and as a consequence of DWF, OIV plays a larger role in water mass transformations.

Finally, each phase of DWF is marked with distinct thermohaline regimes: during preconditioning, the basin-scale thermohaline circulation is fed by exchanges with the Algerian basin. During intense mixing, surface heat fluxes trigger deep convection and internal mixing largely determines the resulting WMDW properties. During restratification, lateral exchanges and internal mixing are enhanced. They feed the basin-scale thermohaline circulation and determine the long-term properties of intermediate and deep waters in the NWMed Sea. During both the preconditioning and the restratification phases, we identified a large contribution of isopycnal mixing to diathermal and diahaline transformations, contributing to heat and salten the WMDW.

4. Discussions

This study focused on NEMOMED12 evaluation, the impact of OIV on DWF, and the identification of processes driving water mass transformations. We now discuss the hypotheses, limitations, and perspectives.

4.1. Model Evaluation

NEMOMED12 has been evaluated using a wide range of observations: from local to basin-scale measurements, focusing on ocean-atmosphere fluxes, ocean hydrological properties and DWF. We can note the lack of a diagnostic on mesoscale activity which impacts both DWF [*Gascard*, 1978] and OIV [*Penduff et al.*, 2011] and might be poorly represented at the eddy-permitting resolution of NEMOMED12. However, the aim of this study is to provide diagnostics on DWF and water mass transformations that are integrated in space and/or in time.

Results regarding NEMOMED12 evaluation show overall its realism in simulating the 2012–2013 DWF events. However, two main biases have been identified: a southward shift of the mixed patch location and a compensating θ-S bias in the new WMDW properties. The first bias is probably related to the representation of the Northern Current and North Balearic front in NEMOMED12, as they dominate the advection of buoyant AW around the DWF area [*Herrmann et al.*, 2008] and constrain the mixed patch location. Given the Northern Current Rossby radius of deformation [*Crepon et al.*, 1982; *Millot*, 1991], the [*Crepon et al.*, 1982; *Millot*, 1991], the Northern Current is expected to be diffusive and therefore wider than observed at NEMOMED12 resolution, which remains to be documented. As for the southward shift of the North Balearic Front, it is visible in the 40 m currents of *Hamon et al.* [2016] hindcast simulation, with a similar NEMOMED12 configuration, as compared to their reanalysis [*Hamon et al.*, 2016, Figure 7]. In particular, we note the presence of an intensified anticyclonic eddy in the Balearic Sea which weakens the North Balearic Front and shifts it to the south. This eddy is no simulations, such a standing eddy was not observed, possibly due to the model initialization, however an anticyclonic circulation anomaly might have developed throughout the simulation. The origin of such a bias remains to be documented.

We showed that the cold bias in the new WMDW is related to ALDERA atmospheric forcing which overestimates strong latent heat flux events. It would probably be reduced by replacing *Louis* [1979] turbulent flux parametrization by a more recent one such as *Fairall et al.* [2003]. As for the fresh bias in the new WMDW, we argued that it originates from a fresh AW bias that develops throughout the simulation at the surface and propagates at depth during DWF. Such a bias might originate from exchanges at the straits of Gibraltar and Sicily or from biases in the WMed Sea circulation. In particular, the Balearic Sea anticyclonic anomaly might bypass the general cyclonic circulation of AW around the basin and advect anomalously fresh AW to the NWMed Sea. The origin of this bias also remains to be documented.

4.2. OIV Estimate

This study quantifies for the first time the impact of OIV on the Mediterranean Sea and on DWF. For this purpose, we perturbed the mesoscale hydrology in summer 2012, assuming that OIV is mostly related to mesoscale activity. Therefore, we made two approximations regarding the spatial scales involved: that smaller scales (e.g., submesoscale) and basin-scale hydrology play a marginal role in OIV. Due to computational costs, the former is unresolved by NEMOMED12 and to our knowledge, its impact on OIV has not been assessed so far.

Now the basin-scale hydrology was fixed in summer 2012 in order to reproduce realistically the 2012–2013 case study. By doing so, the large-scale OIV was canceled by construction. However, a recent study [*Sérazin et al.*, 2015] suggests the large impact of OIV at scales up to ∼500 km, which is the approximate size of the NWMed Sea. Therefore, in an uninitialized configuration, the basin-scale OIV might contribute to increase the total OIV. This issue is intimately related to timescales as the reverse energy cascade between mesoscale and basin-scale OIV takes place at interannual timescales [*Sérazin et al.*, 2015]. We can expect an increase of OIV at interannual timescales as a result of this inverse cascade. We documented an increase of OIV through time in NEMOMED12 which is consistent with this prediction.

Regarding mesoscale, NEMOMED12 only partially resolves it due to the low stratification in the NWMed Sea. Similar studies will have to be conducted with eddy-resolving models to determine NEMOMED12 realism. However, the largest mesoscale structures are resolved by NEMOMED12 and they also have the largest stratification signature: it can be assumed that such mesoscale structures dominate the OIV impact on DWF. In addition, results regarding the sea level OIV at the global scale showed very similar results at eddy-permitting and eddy-resolving resolutions [*Penduff et al.*, 2014].

Finally, the ensemble size responds to the constraints of limiting computational costs and documenting OIV. We used a 10 member ensemble whereas previous studies used 50 members [*Penduff et al.*, 2011, 2014; *Grégorio et al.*, 2015; *Sérazin et al.*, 2015, 2016]. Unfortunately, due to computational costs, we could not increase the ensemble size. Further work should be done to determine the minimum ensemble size for which the OIV statistics converge.

4.3. Water Mass Transformations

Finally, we focused on water mass transformation diagnostics. We identified the large role played by lateral exchanges with the Algerian basin during preconditioning and restratification. They feed the Mediterranean thermohaline circulation. However, we did not establish the link between these exchanges and the restratification of the DWF area, that is the buoyancy advection. It would be interesting to link such exchanges to the DWF area restratification, which impacts the magnitude and properties of deep convection.

We also identified the large role played by internal mixing in all phases: it largely determines the new WMDW properties during the intense mixing phases, and it also impacts the long-term intermediate and deep water properties during preconditioning and restratification. However, the water mass transformation diagnostic only gives access to a basin-scale internal mixing rate. It would be interesting to identify the regions where such mixing occurs. In particular, it would allow to determine if internal mixing during DWF is mostly vertical (due to the mixed layer deepening) or horizontal (due to mixing at the boundaries of the mixed patch).

Also, we identified for the first time a large isopycnal mixing during preconditioning and restratification. Both the WMDW and LIW are involved in this mixing, which is enhanced during the restratification phase. The question of its spatial distribution and its origin remains open. In NEMOMED12, it might be generated by explicitly resolved mesoscale eddies or by their parametrization in the isoneutral mixing coefficient. In particular, the isoneutral coefficient value is likely to impact highly the magnitude of modeled isopycnal water mass transformations. As discussed by *McDougall et al.* [2014], the low interior ocean dissipation rate provides a strong physical rationale for implementing an isoneutral mixing coefficient for tracers in numerical models. However, no direct isoneutral mixing measurement is available to constrain its value. The realism of the isopycnal mixing coefficient and the sensitivity of results to its value therefore remain to be documented.

Finally, because of the density dependency on pressure, there is in theory no equivalence between isopycnal and isoneutral mixing. The former has been determined from a surface-referenced potential density σ_0

which does not follow isoneutral surfaces (of neutral buoyancy) far from the surface. All diagnostics related to σ_0 are impacted by this source of error. However, σ_0 is by far the most used density variable in the Mediterranean Sea, which facilitates the interpretation of results and the comparison with previous studies. In addition, no neutral density variable [*Jackett and McDougall*, 1997] has been implemented in the Mediterranean Sea, and such a work would be useful to limit errors in density-related diagnostics.

5. Conclusions

Winter 2012-2013 was an intense and well-documented dense water formation (DWF) period in the northwestern Mediterranean (NWMed) Sea. In this study, we use an ensemble eddy-permitting simulation with the regional model NEMOMED12 from summer 2012 to summer 2013 in order to evaluate its realism in representing the DWF process, to assess the impact of ocean intrinsic variability (OIV) in DWF and to characterize the physical processes that drive water mass transformations. For that purpose, we use a perturbed initial state ensemble with a common basin-scale initial hydrology deduced from observations in summer 2012 and a perturbed mesoscale hydrology deduced from a twin hindcast simulation.

We first characterize and evaluate the chronology and geography of DWF, we quantify the DWF and restratification rate and we assess the main hydrological transformations involved. NEMOMED12 reproduces realistically the well-documented and intense 2012–2013 DWF event. The chronology of the event and its surface signature are well reproduced with three main intense vertical mixing episodes between late January and mid-March. Accurate initial hydrology and surface forcing chronology are necessary ingredients to reproduce this event. Its location compares overall well with observations, with a mixed patch mostly off the Gulf of Lions, although too much to the south. The DWF magnitude is estimated with complementary methods: the DWF area reaches up to $28,000 \, km^2$ when deduced from the mixed patch area (A_{MLD}) and $45,000 \, km^2$ from the cold intermediate water area (A_{cold}). The DWF rate reaches 1.8 Sv when deduced from the mixed patch volume (V_{MLD}) and 1.7 Sv from the dense water volume transformations (V_{dens}). Observations suggest either that NEMOMED12 is realistic (A_{MLD}), that it overestimates (A_{cold} and V_{MLD}) or underestimates (V_{dens}) DWF. The discrepancies are related to the different physical nature of each diagnostic and to different observation periods. The restratification volume reaches $-1.4^{13} m^3$ in NEMOMED12 during spring, being underestimated by more than 50%. In terms of hydrology, the Western Mediterranean Deep Water densification and associated diapycnal transformation rate is realistic in NEMOMED12. However, the thermohaline signature is mostly a cooling in NEMOMED12, but a warming and saltening in observations. This is consistent with the atmospheric forcing ALDERA which was shown to be realistic in terms of surface parameters and chronology, but which overestimates the net heat loss mostly due to the latent heat flux.

The OIV impacts largely the DWF event geography and properties locally, especially in the open-sea. More than 50% of the modeled mixed patch surface is impacted by OIV. It is however low along the northern shelf, which is consistent with the impact of bathymetry slope on eddy fluxes. In addition, the OIV was shown to impact marginally the time and space-integrated DWF rate, reaching typically 3–5% of the modeled DWF rate. Finally, we have identified an increase of OIV as a function of time, suggesting that it could impact largely DWF at interannual timescales.

We then assessed the physical mechanisms that drive water mass transformations in the density, salinity, and temperature dimensions. Each phase of DWF is dominated by distinct thermohaline regimes: during preconditioning, the basin-scale thermohaline circulation is fed by exchanges with the Algerian basin where the deep water is exported and replaced by Levantine Intermediate Water. We also identify a mostly isopycnal internal mixing of deep water which increases their salinity and temperature. During the intense mixing phase, surface heat fluxes generate a large diathermal and diapycnal flux which triggers deep convection, while surface water fluxes play a secondary role in water mass transformations. However, internal mixing largely determines the resulting deep water properties, while eroding a large volume of intermediate water. During restratification, lateral exchanges and internal mixing are enhanced. They feed the basin-scale thermohaline circulation and determine the long-term properties of intermediate and deep waters in the NWMed Sea. Internal mixing is shown to also have a large isopycnal component which contributes to warm and salten deep waters whereas it cools and freshens intermediate waters. Therefore internal mixing plays a large role in water mass transformations throughout DWF and it ultimately determines the intermediate and deep water properties in the NWMed Sea.
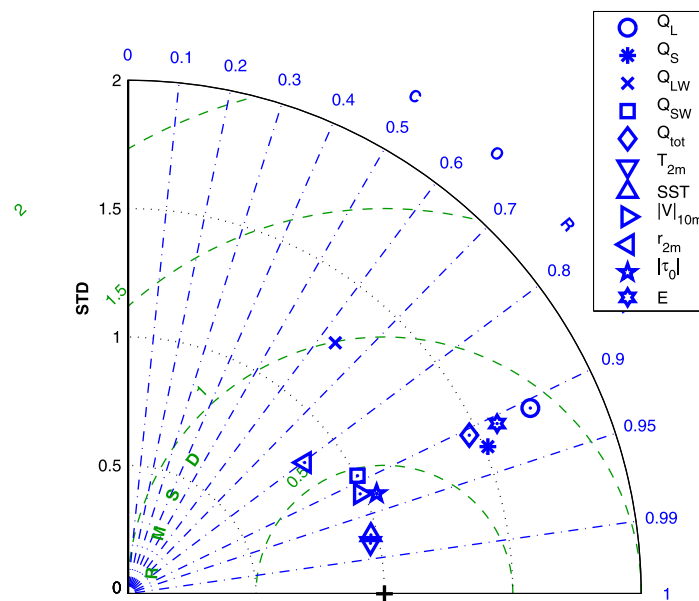
Figure 12. Normalized daily temporal Taylor diagram of ALDERA surface parameters and turbulent fluxes at LION buoy with respect to observations or reconstructions for turbulent fluxes. The black cross represents observations.

Appendix A: Evaluation of ALDERA Above the NWMed Sea

We focus on the evaluation of ALDERA surface forcing (12 km, 3 h resolution) with fluxes estimated locally at the LION moored buoy as well as with fluxes that where retrieved over a much larger area at fine temporal (1 h) and spatial scale (0.0° longitude x 0.04° latitude) by an inverse method (Caniaux et al., in revision). They produced an annual surface heat and water flux data set derived from the closure of the heat and water budgets observed in the area. The inverse method used relies on numerous simulations of a single-column model optimized by a genetic algorithm and able to minimize a cost function taking into account all the observations collected during one year in the NWMed basin. The surface flux data set over the area 0°E-12°E, 38°N-44°N and the period between 1 August 2012 and 30 June 2013 is considered here as a reference.

Figure 12 displays the normalized temporal daily Taylor diagram [*Taylor*, 2001] of surface parameters and heat fluxes at LION buoy modeled by ALDERA during the oceanic run period (1 August 2012 to 30 June 2013) with respect to observations or reconstructions from observations for turbulent fluxes. Note that the Taylor diagram gives no information on the model mean bias. It is normalized with observations for both the STD and RMSD. Three groups of surface variables clearly appear in this diagram: first, the air (T_{2m}) and sea (SST) surface temperatures, the surface wind $|V|_{10m}$ and wind stress $|\tau_0|$ have high correlations with observations (>0.9), similar STDs (factor $0.9-1.1$) and therefore low RMSDs (below 0.5). They are well represented by ALDERA, and this can be related to the boundary forcings of ALDERA by ERA-Interim reanalysis, both at the surface for the SST and at the lateral boundaries for all atmospheric prognostic variables. Second, the turbulent sensible (Q_S) and latent (Q_L) heat fluxes, the total heat flux (Q_{tot}) and the evaporation E are well-represented in terms of correlation (>0.9), but relatively poorly in terms of STD, with overestimates of 45–70% of the variability, and therefore larger RMSDs (0.7–0.9). ALDERA uses Louis turbulent flux parametrization [*Louis*, 1979] which deduces from surface variables the Q_S, Q_L, the evaporation rate, and the surface wind stress. It might cause the STD overestimation for all those variables, which has already been identified at the Mediterranean basin-scale [*Hamon et al.*, 2016]. Finally, the near-surface moisture r_{2m}, the longwave (Q_{LW}) and shortwave (Q_{SW}) heat fluxes have relatively low STD biases (factor $0.8-1.3$) but lower correlations with observations (<0.9), which causes larger RMSDs (0.5–1). This suggests that average biases are low but the chronology of those parameters does not compare well with observations in ALDERA. It can be related to the high dependency of all these parameters to the mesoscale vertical physics determining moisture and clouds.

Figure 13 displays for all previous parameters the quantile-quantile plot of daily modeled values (blue dots) with respect to observed or reconstructed values (black bissectrice), and it specifies their average bias and temporal correlation. The 5th (p5) to 95th (p95) model percentiles are displayed with respect to observations, which allows to identify the causes of model biases. Regarding the first group of highly accurate parameters, T_{2m} has a low warm bias at all quantiles of average $+0.4°$C. The SST has no average bias but the quantile distribution is stair-like due to the monthly averaging of ERA-Interim SST in ALDERA. The $SST-T_{2m}$ (not shown) therefore has a low negative bias at all quantiles, of average $-0.5°$C. The near-surface wind
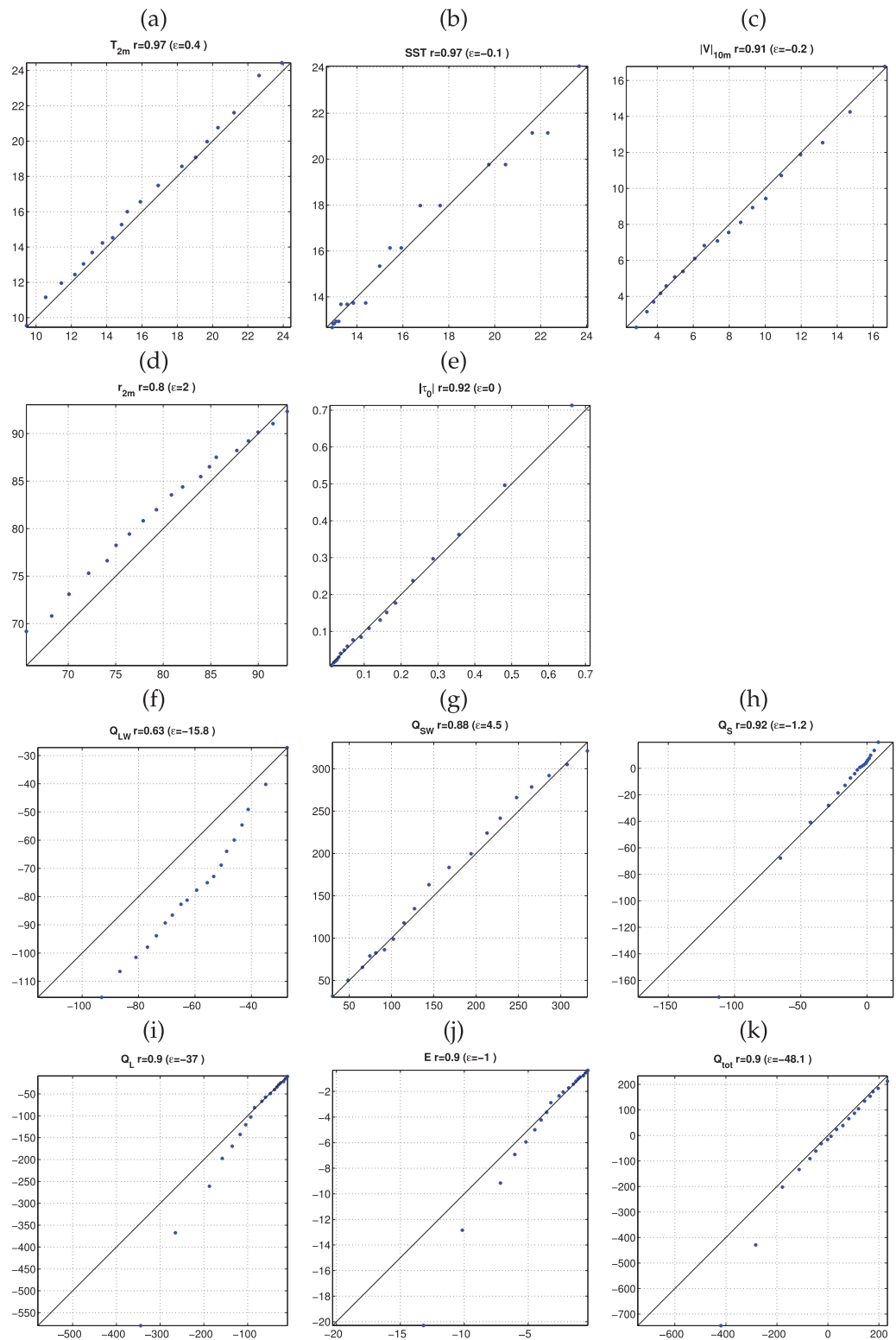
Figure 13. Quantile-quantile plot of daily modeled surface parameters at LION between 1 August 2012 and 30 June 2013 with respect to observations or reconstructions for turbulent fluxes. Blue dots represent comparisons between model in the y axis and observations in the x axis for all 1/20iles between p5 and p95, the black bissectrice represents a null bias. The time correlation (r) and mean bias (ϵ) are also displayed.
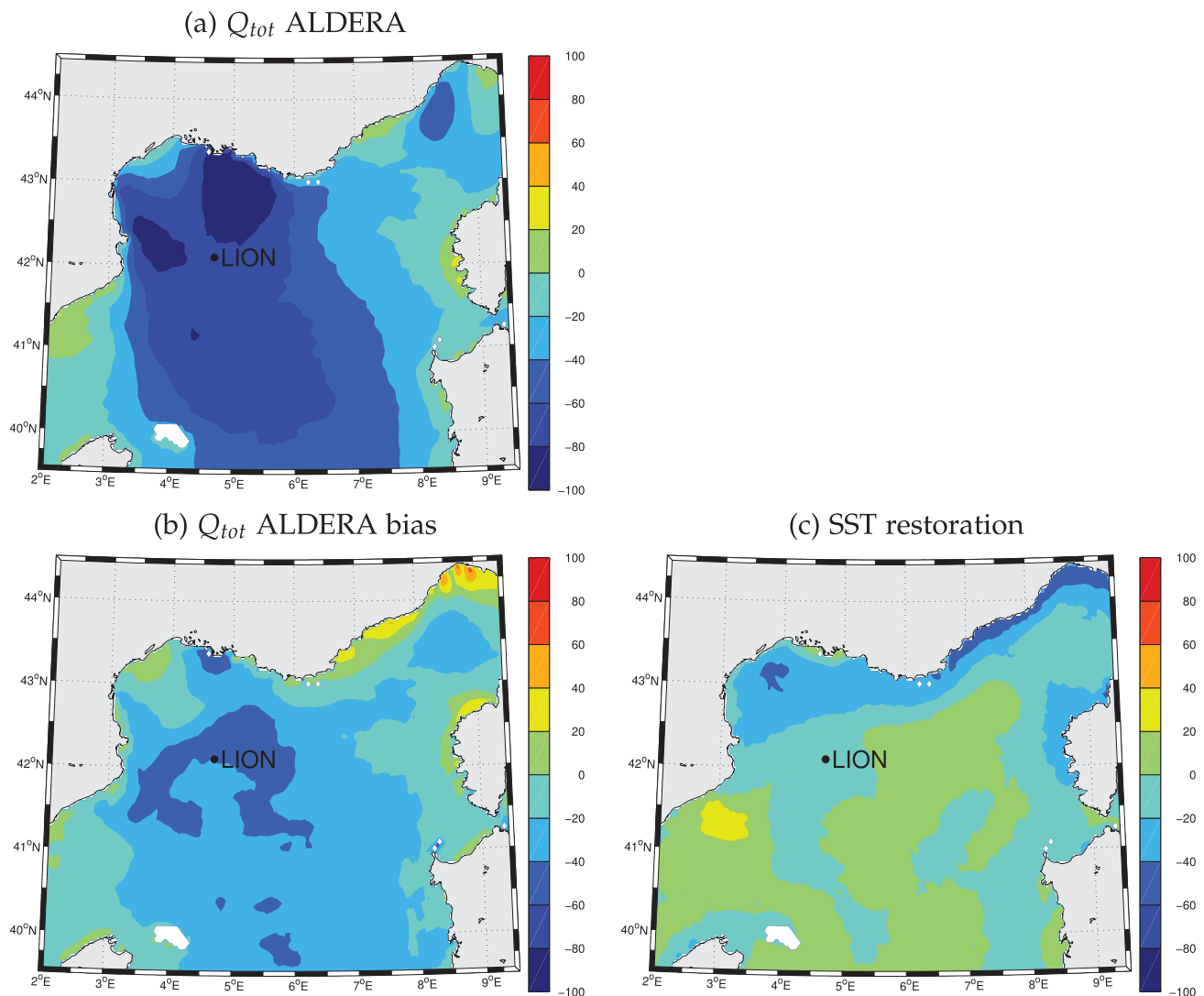
Figure 14. (a) Mean net surface heat flux Q_{tot} (W/m²) in ALDERA, on average between 1 August 2012 and 30 June 2013. (b) Same as Figure 14a, bias with respect to Caniaux et al. (in revision) reconstruction. (c) Mean surface heat flux restoration over the same period induced by the Newtonian sea surface temperature (SST) damping in NEMOMED12.

$|V|_{10m}$ has almost no bias even for extreme values and only an average bias of -0.2 m/s, confirming *Herrmann et al.* [2011] results. Finally, the surface wind stress $|\tau_0|$ has no average bias. Now looking at the second group of parameters with too high STDs, they are all overestimated on average with biases of -1.2 W/m², -37 W/m², -48.1 W/m², and -1 mm/d for, respectively, Q_S, Q_L, Q_{tot}, and E. In all cases, it is related to extreme values (percentiles p5 to p25). In particular, Q_{tot} bias at LION is dominated at 80% by Q_L bias. The low Q_S bias is due to the compensation between a negative bias for high-flux regimes related to the turbulent flux formulation and a positive bias for low and positive flux regimes related to a too warm near-surface atmosphere. As for the third group of variables with lower correlation, r_{2m} has a low bias of 2%, lower than the instrumental accuracy (M. N. Bouin, personal communication). Q_{LW} is too low by -15.8 W/m² on average and at all quantiles, due to a too low downward Q_{LW} (not shown), and Q_{SW} is slightly too high on average ($+4.5$ W/m²): both biases might be caused by a too low atmospheric optical depth likely related to a too low cloud cover in ALDERA and they are responsible for the remaining 20% of Q_{tot} bias.

Figure 14 displays Q_{tot} average over the simulation period in ALDERA, its bias with regard to Caniaux et al. (in revision) reconstruction and the average heat flux correction corresponding to the SST restoration in NEMOMED12 (see section 2.1). The model Q_{tot} has a negative average over the 11 month period, consistent with an average heat loss in the Mediterranean Sea compensated by a heat intake at the Gibraltar strait and

with the lack of one summer month in the period. The heat loss is highest off and south of the Gulf of Lions with two jets that are the surface signatures of Mistral and Tramontane regional wind pathways [*Herrmann et al.*, 2011]. Their location is in qualitative agreement with Caniaux et al. (in revision) reconstruction (spatial correlation r = 0.78). The average heat loss reaches up to $-100\,\mathrm{W/m^2}$ below the Mistral jet at $(43°\mathrm{N}, 5°\mathrm{E})$. A secondary heat loss pattern is visible in the Ligurian Sea and can be related to the northeasterly wind pattern off the French Riviera Caniaux et al. (in revision). The model bias with respect to Caniaux et al. (in revision) heat flux reconstruction is negative on average similarly as LION buoy, although it is highest below the Mistral and Tramontane pathways (Figure 14b). Therefore, LION buoy heat flux is representative of the average NWMed basin heat flux, although it is stronger on average. The average heat flux bias is $\sim\!-20$ $\mathrm{W/m^2}$ over the basin. Finally, the SST restoration acts as a flux correction term but it is negative on average $(-3.4\,\mathrm{W/m^2})$, because of strong negative values along the northern coast. The coastal—open-sea opposite dipole of restoration is related to high-resolution SST gradients in NEMOMED12 which are damped towards the low-resolution ERA-Interim SST. However, most of the heat flux bias is not compensated by the SST restoration term, therefore the oceanic simulations still receive excessive cooling over the period.

To conclude, the atmospheric forcing evaluation at LION reveals a high accuracy of thermal and dynamic parameters, but an overestimation of turbulent cooling and the resulting total cooling and evaporation and poorer representation of the parameters related to moisture and clouds in terms of chronology. The resulting total heat flux has an accurate chronology but it overestimates high-flux values due to the *Louis* [1979] turbulent flux parametrization. Results at LION resemble those at the basin-scale, although the average total heat flux bias is twice as high at LION as the whole NWMed Sea. Also, ALDERA evaluation at the basin-scale reveals the realism of the spatial patterns of modeled mean heat fluxes. To our knowledge, no better high-resolution atmospheric forcing is available over the whole Mediterranean Sea in this period [*Estournel et al.*, 2016a; *Leger et al.*, 2016].

References

ARGO (2000), Argo float data and metadata from Global Data Assembly Centre (ARGO GDAC), SEANOE. [Available at http://doi.org/10.17882/42182.]

Auger, P., C. Estournel, C. Ulses, L. Stemmann, S. Somot, and F. Diaz (2014), Interannual control of plankton ecosystem in a deep convection area as inferred from a 30-year 3D modeling study: Winter mixing and prey/predator interactions in the NW Mediterranean, *Prog. Oceanogr.*, *124*, 12–27, doi:10.1016/j.pocean.2014.04.004.

Badin, G., R. G. Williams, and J. Sharples (2010), Water-mass transformation in the shelf seas, *J. Mar. Res.*, *68*(2), 189–214.

Badin, G., R. G. Williams, Z. Jing, and L. Wu (2013), Water mass transformations in the southern ocean diagnosed from observations: Contrasting effects of air–sea fluxes and diapycnal mixing, *J. Phys. Oceanogr.*, *43*(7), 1472–1484.

Balmaseda, M. A., K. Mogensen, and A. T. Weaver (2013), Evaluation of the ECMWF ocean reanalysis system oras4, *Q. J. R. Meteorol. Soc.*, *139*(674), 1132–1161.

Barnier, B., L. Siefridt, and P. Marchesiello (1995), Thermal forcing for a global ocean circulation model using a three year climatology of ECMWF analyses, *J. Mar. Syst.*, *6*(4), 363–380.

Barnier, B., et al. (2006), Impact of partial steps and momentum advection schemes in a global ocean circulation model at eddy-permitting resolution, *Ocean Dyn.*, *56*, 543–567.

Béranger, K., Y. Drillet, M.-N. Houssais, P. Testor, R. Bourdallé-Badie, B. Alhammoud, A. Bozec, L. Mortier, P. Bouruet-Aubertot, and M. Crépon (2010), Impact of the spatial distribution of the atmospheric forcing on water mass formation in the Mediterranean Sea., *J. Geophys. Res.*, *115*, C12041, doi:10.1029/2009JC005648.

Beuvier, J., K. Beranger, C. L. Brossier, S. Somot, F. Sevault, Y. Drillet, R. Bourdalle-Badie, N. Ferry, and F. Lyard (2012), Spreading of the western mediterranean deep water after winter 2005: Time scales and deep cyclone transport, *J. Geophys. Res.*, *117*, C07022, doi:10.1029/2011JC007679.

Blumsack, S. L., and P. Gierasch (1972), Mars: The effects of topography on baroclinic instability, *J. Atmos. Sci.*, *29*(6), 1081–1089.

Bosse, A., P. Testor, L. Mortier, L. Prieur, V. Taillandier, F. d'Ortenzio, and L. Coppola (2015), Spreading of Levantine intermediate waters by submesoscale coherent vortices in the northwestern Mediterranean sea as observed with gliders, *J. Geophys. Res. Oceans*, *120*, 1599–1622, doi:10.1002/2014JC010263.

Bosse, A., et al. (2016), Scales and dynamics of submesoscale coherent vortices formed by deep convection in the northwestern mediterranean sea, *J. Geophys. Res. Oceans*, *121*, 7716–7742, doi:10.1002/2016JC012144.

Castellari, S., N. Pinardi, and K. Leaman (2000), Simulation of the water mass formation processes in the Mediterranean Sea: Influence of the time frequency of the atmospheric forcing, *J. Geophys. Res.*, *105*(C10), 24,157–24,181, doi:10.1029/2000JC900055.

Colin, J., M. Déqué, R. Radu, and S. Somot (2010), Sensitivity study of heavy precipitation in limited area model climate simulations: Influence of the size of the domain and the use of the spectral nudging technique, *Tellus Ser. A*, *62*, 591–604.

Conan, P. (2013), DEWEX-MERMEX 2013 LEG2 cruise, le Suroit R/V, technical report, doi:10.17600/13020030. [Available at http://campagnes.flotteoceanographique.fr/campagnes/13020030/.]

Crepon, M., L. Wald, and J. M. Monget (1982), Low-frequency waves in the Ligurian sea during December 1977, *J. Geophys. Res.*, *87*(C1), 595–600, doi:10.1029/JC087iC01p00595.

Demirov, E. K., and N. Pinardi (2007), On the relationship between the water mass pathways and eddy variability in the western mediterranean sea, *J. Geophys. Res.*, *112*, C02024, doi:10.1029/2005JC003174.

Durrieu de Madron, X., et al. (2013), Interaction of dense shelf water cascading and open-sea convection in the northwestern Mediterranean during winter 2012, *Geophys. Res. Lett.*, *40*, 1379–1385, doi:10.1002/grl.50331.

Escudier, R., J. Bouffard, A. Pascual, P.-M. Poulain, and M.-I. Pujol (2013), Improvement of coastal and mesoscale observation from space: Application to the northwestern mediterranean sea, *Geophys. Res. Lett.*, *40*, 2148–2153, doi:10.1002/grl.50324.

Estournel, C., et al. (2016a), High resolution modelling of dense water formation in the north-western mediterranean during winter 2012-2013: Processes and budget, *J. Geophys. Res. Oceans*, *121*, 5367–5392, doi:10.1002/2016JC011935.

Estournel, C., et al. (2016b), Hymex-sop2, the field campaign dedicated to dense water formation in the north-western mediterranean, *Oceanography*, *29*(4), 196–206.

Fairall, C., E. F. Bradley, J. Hare, A. Grachev, and J. Edson (2003), Bulk parameterization of air-sea fluxes: Updates and verification for the coarse algorithm, *J. Clim.*, *16*(4), 571–591.

Gascard, J.-C. (1978), Mediterranean deep water formation, baroclinic eddies and ocean eddies, *Oceanol. Acta*, *1*(3), 315–330.

Gaspar, P., Y. Gregoris, and J. Lefèvre (1990), A simple eddy kinetic energy model for simulations of the oceanic vertical mixing: tests at station Papa and long-term upper ocean study site, *J. Geophys. Res.*, *95*(C9), 16,179–16,193.

Gent, P., and J. McWilliams (1990), Isopycnal mixing in ocean circulation models, *J. Phys. Oceanogr.*, *20*, 150–155.

Grégorio, S., T. Penduff, G. Sérazin, J.-M. Molines, B. Barnier, and J. Hirschi (2015), Intrinsic variability of the Atlantic meridional overturning circulation at interannual-to-multidecadal time scales, *J. Phys. Oceanogr.*, *45*(7), 1929–1946.

Groeskamp, S., J. D. Zika, T. J. McDougall, B. M. Sloyan, and F. Laliberté (2014a), The representation of ocean circulation and variability in thermodynamic coordinates, *J. Phys. Oceanogr.*, *44*(7), 1735–1750.

Hamon, M., et al. (2016), Design and validation of MEDRYS, a mediterranean sea reanalysis over the period 19922013, *Ocean Sci.*, *12*(2), 577–599, doi:10.5194/os-12-577-2016.

Herrmann, M., and S. Somot (2008), Relevance of ERA40 dynamical downscaling for modeling deep convection in the Mediterranean Sea, *Geophys. Res. Lett.*, *35*, L04607, doi:10.1029/2007GL032442.

Herrmann, M., S. Somot, F. Sevault, C. Estournel, and M. Déqué (2008), Modeling the deep convection in the Northwestern Mediterranean sea using an eddy-permitting and an eddy-resolving model: case study of winter 1986-87, *J. Geophys. Res.*, *113*, C04011, doi:10.1029/2006JC003991.

Herrmann, M., F. Sevault, J. Beuvier, and S. Somot (2010), What induced the exceptional 2005 convection event in the northwestern Mediterranean basin? Answers from a modeling study, *J. Geophys. Res.*, *115*, C08029, doi:10.1029/2009JC005749.

Herrmann, M., S. Somot, S. Calmanti, C. Dubois, and F. Sevault (2011), Representation of spatial and temporal variability of daily wind speed and of intense wind events over the Mediterranean Sea using dynamical downscaling: Impact of the regional climate model configuration, *Nat. Hazards Earth Syst. Sci.*, *11*, 1983–2001, doi:10.5194/nhess-11-1983-2011.

Herrmann, M., C. Estournel, F. Diaz, and F. Adloff (2014), Impact of climate change on the Northwestern Mediterranean Sea pelagic planktonic ecosystem and associated carbon cycle., *J. Geophys. Res.*, *119*, 5815–5836, doi:10.1002/2014JC010016.

Hieronymus, M., J. Nilsson, and J. Nycander (2014), Water mass transformation in salinity–temperature space, *J. Phys. Oceanogr.*, *44*(9), 2547–2568.

Houpert, L., et al. (2016), Observations of open-ocean deep convection in the northwestern mediterranean sea: Seasonal and interannual variability of mixing and deep water masses for the 2007-2013 period, *J. Geophys. Res. Oceans*, *121*, 8139–8171, doi:10.1002/2016JC011857.

Iselin, C. (1939), The influence of vertical and lateral turbulence on the characteristics of the waters at mid-depths, *Eos Trans. AGU*, *20*(3), 414–417.

Iudicone, D., G. Madec, and T. J. McDougall (2008), Water-mass transformations in a neutral density framework and the key role of light penetration, *J. Phys. Oceanogr.*, *38*(7), 1357–1376, doi:10.1175/2007JPO3464.1.

Jackett, D. R., and T. J. McDougall (1997), A neutral density variable for the world's oceans, *J. Phys. Oceanogr.*, *27*(2), 237–263.

Lascaratos, A. (1993), Estimation of deep and intermediate water mass formation rates in the Mediterranean sea, *Deep Sea Res., Part II*, *40*(6), 1327–1332.

Leaman, K. D., and F. Schott (1991), Hydrographic structure of the convection regime in the Gulf of Lions: Winter 1987, *J. Phys. Oceanogr.*, *21*, 575–597.

Leger, F., C. Lebeaupin Brossier, H. Giordani, T. Arsouze, J. Beuvier, M.-N. Bouin, É. Bresson, V. Ducrocq, N. Fourrié, and M. Nuret (2016), Dense water formation in the north-western mediterranean area during hymex-sop2 in 1/36 ocean simulations: Sensitivity to initial conditions, *J. Geophys. Res. Oceans*, *121*, 5549–5569, doi:10.1002/2015JC011542.

L'Hévéder, B., L. Li, F. Sevault, and S. Somot (2013), Interannual variability of deep convection in the northwestern mediterranean simulated with a coupled AORCM, *Clim. Dyn.*, *41*(3-4), 937–960, doi:10.1007/s00382-012-1527-5.

Louis, J.-F. (1979), A parametric model of vertical eddy fluxes in the atmosphere, *Boundary Layer Meteorol.*, *17*(2), 187–202, doi:10.1007/BF00117978.

Ludwig, W., E. Dumont, M. Meybeck, and S. Heussner (2009), River discharges of water and nutrients to the mediterranean and black sea: major drivers for ecosystem changes during past and future decades?, *Prog. Oceanogr.*, *80*(3), 199–217.

Lyard, F., F. Lefevre, T. Letellier, and O. Francis (2006), Modelling the global ocean tides: Modern insights from fes2004, *Ocean Dyn.*, *56*(5), 394–415, doi:10.1007/s10236-006-0086-x.

Madec, G. (2008), NEMO ocean engine, note du Pole de modélisation, Inst. Pierre-Simon Laplace (IPSL), France.

Marchesiello, P., X. Capet, C. Menkes, and S. Kennan (2011), Submesoscale dynamics in tropical instability waves, *Ocean Modell.*, *39*(12), 31–46, doi:10.1016/j.ocemod.2011.04.011.

Marshall, J., and F. Schott (1999), Open-ocean convection: observations, theory, and models, *Rev. Geophys.*, *37*(1), 1–64.

Maze, G., G. Forget, M. Buckley, J. Marshall, and I. Cerovecki (2009), Using transformation and formation maps to study the role of air-sea heat fluxes in north Atlantic eighteen degree water formation, *J. Phys. Oceanogr.*, *39*(8), 1818–1835.

McDougall, T. J. (1987), Neutral surfaces, *J. Phys. Oceanogr.*, *17*(11), 1950–1964.

McDougall, T. J., S. Groeskamp, and S. M. Griffies (2014), On geometrical aspects of interior ocean mixing, *J. Phys. Oceanogr.*, *44*(8), 2164–2175.

MEDOC-Group (1970), Observations of formation of deep-water in the Mediterranean Sea, *Nature*, *227*, 1037–1040.

Mertens, C., and F. Schott (1998), Interannual variability of deep-water formation in the Northwestern Mediterranean, *J. Phys. Oceanogr.*, *28*, 1410–1424.

Millot, C. (1991), Mesoscale and seasonal variabilities of the circulation in the Western Mediterranean, *Dyn. Atm. Oceans*, *15*, 179–214.

Millot, C., and I. Taupier-Letage (2005), Additional evidence of LIW entrainment across the Algerian subbasin by mesoscale eddies and not by a permanent westward flow, *Prog. Oceanogr.*, *66*(2–4), 231–250.

Montgomery, R. B. (1958), Water characteristics of Atlantic ocean and of world ocean, *Deep Sea Res.*, *5*(2–4), 134–148.

Myers, P. G., and C. Donnelly (2008), Water mass transformation and formation in the labrador sea, *J. Clim.*, *21*(7), 1622–1638.

Nilsson, E. D. (1996), Planetary boundary layer structure and air mass transport during the international arctic ocean expedition 1991, *Tellus Ser. B*, *48*(2), 178–196.

Penduff, T., M. Juza, B. Barnier, J. Zika, W. K. Dewar, A.-M. Treguier, J.-M. Molines, and N. Audiffren (2011), Sea level expression of intrinsic and forced ocean variabilities at interannual time scales, *J. Clim.*, *24*(21), 5652–5670.

Penduff, T., B. Barnier, L. Terray, L. Bessières, G. Sérazin, S. Gregorio, J. Brankart, M. Moine, J. Molines, and P. Brasseur (2014), Ensembles of eddying ocean simulations for climate, in *CLIVAR WGOMD Workshop on High*, 26 pp.

Pennel, R., A. Stegner, and K. Béranger (2012), Shelf impact on buoyant coastal current instabilities, *J. Phys. Oceanogr.*, *42*(1), 39–61.

Prieur, L., G. Caniaux, F. D'Ortenzio, H. Lavigne, and H. Giordani (2010), Rapport prosat, technical report. [Available at ftp://oceane.obs-vlfr.fr/pub/prieur/RW/RapportFinal%20Prosat.pdf.]

Rugenstein, M., M. Winton, R. J. Stouffer, S. M. Griffies, and R. Hallberg (2013), Northern high-latitude heat budget decomposition and transient warming, *J. Clim.*, *26*, 609–621.

Sannino, G., M. Herrmann, A. Carillo, V. Rupolo, V. Ruggiero, V. Artale, and P. Heimbach (2009), An eddy-permitting model of the mediterranean sea with a two-way grid refinement at the strait of Gibraltar, *Ocean Modell.*, *30*(1), 56–72, doi:10.1016/j.ocemod.2009.06.002.

Santinelli, C., et al. (2013), Influence of stratification on marine dissolved organic carbon (doc) dynamics: The mediterranean sea case, *Prog. Oceanogr.*, *119*, 68–77.

Schott, F., M. Visbeck, U. Send, J. Fisher, L. Stramma, and Y. Desaubies (1996), Observations of deep convection in the Gulf of Lions, northern Mediterranean, during the winter of 1991/1992, *J. Phys. Oceanogr.*, *26*, 505–524.

Schröder, K., G.-P. Gasparini, M. Tangherlini, and M. Astraldi (2006), Deep and intermediate water in the western Mediterranean under the influence of the Eastern Mediterranean Transient, *Geophys. Res. Lett.*, *33*, L21607, doi:10.1029/2006GL027121.

Sérazin, G., T. Penduff, S. Grégorio, B. Barnier, J.-M. Molines, and L. Terray (2015), Intrinsic variability of sea level from global ocean simulations: Spatiotemporal scales, *J. Clim.*, *28*(10), 4279–4292.

Sérazin, G., B. Meyssignac, T. Penduff, L. Terray, B. Barnier, and J.-M. Molines (2016), Quantifying uncertainties on regional sea level change induced by multidecadal intrinsic oceanic variability, *Geophys. Res. Lett.*, *43*, 8151–8159, doi:10.1002/2016GL069273.

Somot, S., F. Sevault, and M. Déqué (2006), Transient climate change scenario simulation of the Mediterranean Sea for the 21st century using a high resolution ocean circulation model, *Clim. Dyn.*, *27*, 1–29, doi:10.1007/s00382-006-0167-z.

Somot, S., et al. (2016), Characterizing, modelling and understanding the climate variability of the deep water formation in the northwestern mediterranean sea, *Clim. Dyn.*, 1–32.

Spall, M. A. (2004), Boundary currents and water mass transformation in marginal seas, *J. Phys. Oceanogr.*, *34*(5), 1197–1213.

Speer, K., and E. Tziperman (1992), Rates of water mass formation in the North Atlantic Ocean, *J. Phys. Oceanogr.*, *22*, 93–104.

Speer, K. G. (1993), Conversion among north Atlantic surface water types, *Tellus Ser. A*, *45*(1), 72–79.

Stanev, E. V., and E. L. Peneva (2001), Regional sea level response to global climatic change: Black sea examples, *Global Planet. Change*, *32*(1), 33–47.

Taillandier, V. (2014), (CTD dataset acquired during the field survey DEWEX), technical report, doi:10.17600/13450110. [Available at ftp://oceane.obs-vlfr.fr/pub/prieur/GC/Dewex2013leg1_leg2_ASCII/DEWEX2013-CTDreport.pdf.]

Tamburini, C., et al. (2013), Deep-sea bioluminescence blooms after dense water formation at the ocean surface, *PLoS ONE*, *8*(7), e67523, doi:10.1371/journal.pone.0067523.

Taylor, K. E. (2001), Summarizing multiple aspects of model performance in a single diagram, *J. Geophys. Res.*, *106*(D7), 7183–7192.

Testor, P. (2013), DEWEX-MERMEX 2013 LEG1 cruise, le Suroit R/V, technical report, doi:10.17600/13020010. [Available at http://campagnes.flotteoceanographique.fr/campagnes/13020010/.]

Testor, P., and J.-C. Gascard (2003), Large-scale spreading of deep waters in the Western Mediterranean Sea by submesoscale coherent eddies, *J. Phys. Oceanogr.*, *33*, 75–87.

Testor, P., L. Coppola, and L. Mortier (2012), 2012 MOOSE-GE cruise, le Suroit R/V, technical report, doi:10.17600/12020030. [Available at http://campagnes.flotteoceanographique.fr/campagnes/12020030/index.htm.]

Testor, P., L. Coppola, and L. Mortier (2013), 2013 MOOSE-GE cruise, Tethys ii R/V, technical report, doi:10.17600/13450110. [Available at http://campagnes.flotteoceanographique.fr/campagnes/13450110/index.htm.]

Testor, P., X. Durrieu de Madron, L. Mortier, F. D'Ortenzio, H. Legoff, D. Dausse, M. Labaste, and L. Houpert (2016), Lion observatory data, technical report, doi:10.17882/44411. [Available at http://campagnes.flotteoceanographique.fr/campagnes/13450110/index.htm.]

Tziperman, E. (1986), On the role of interior mixing and air-sea fluxes in determining the stratification and circulation of the oceans, *J. Phys. Oceanogr.*, *16*, 680–693.

Tziperman, E., and K. Speer (1994), A study of water mass transformation in the Mediterranean Sea: analysis of climatological data and a simple three-box model, *Dyn. Atm. Oceans*, *21*, 53–82.

Vörösmarty, C., B. Fekete, and B. Tucker (1996), *Global River Discharge Database, RivDis*, UNESCO, Paris.

Waldman, R., et al. (2016), Estimating dense water volume and its evolution for the year 2012-2013 in the north-western Mediterranean sea: An observing system simulation experiment approach, *J. Geophys. Res. Oceans*, *121*, 6696–6716, doi:10.1002/2016JC011694.

Walin, G. (1977), A theoretical framework for the description of estuaries, *Tellus*, *29*(2), 128–136.

Walin, G. (1982), On the relation between sea-surface heat flow and the thermal circulation in the ocean, *Tellus*, *34*, 187–195.

Winton, M., S. M. Griffies, B. L. Samuels, J. L. Sarmiento, and T. L. Frolicher (2013), Connecting changing ocean circulation with changing climate, *J. Clim.*, *26*, 2268–2278.

Worthington, L. (1981), The water masses of the world ocean: Some results of a fine-scale census, in *Evolution of Physical Oceanography*, edited by B. A. Warren and C. Wunsch, Ch. 2, pp. 42–69, MIT Press, Cambridge, Mass.